

# The enigmatic multiple star VV Ori

Edwin Budding<sup>1,2</sup>, John Southworth<sup>3\*</sup>, Krešimir Pavlovski<sup>4</sup>, Michael D. Rhodes<sup>5</sup>, Wu Zihao<sup>6</sup>, Tom Love<sup>7</sup>, Mark G. Blackford<sup>8</sup>, Timothy S. Banks<sup>9,10</sup>, & Murray Alexander<sup>11</sup>

<sup>1</sup>*Carter Observatory, 40 Salamanca Road, Kelburn, Wellington 6012, New Zealand*

<sup>2</sup>*School of Chemical & Physical Sciences, Victoria University of Wellington, PO Box 600, Wellington 6140, New Zealand*

<sup>3</sup>*Astrophysics Group, Keele University, Staffordshire, ST5 5BG, UK*

<sup>4</sup>*Department of Physics, Faculty of Science, University of Zagreb, Bijenička cesta 32, 10000 Zagreb, Croatia*

<sup>5</sup>*Brigham Young University, Provo, Utah 84602, USA*

<sup>6</sup>*Dept. Statistics & Data Science, National University of Singapore, 6 Science Drive 2, Singapore 117546*

<sup>7</sup>*Variable Stars South, RASNZ, PO Box 3181, Wellington 6011, New Zealand*

<sup>8</sup>*Variable Stars South, Congarinni Observatory, Congarinni, NSW, 2447, Australia*

<sup>9</sup>*Nielsen, 675 6th Ave, New York, NY 10011, USA*

<sup>10</sup>*Dept. of Physical Science & Engineering, Harper College, 1200 W Algonquin Rd, Palatine, Illinois 60067, USA*

<sup>11</sup>*Physics Department, University of Winnipeg, 515 Portage Avenue, Winnipeg R3B 2E9, Canada*

Accepted 2023 November 10. Received 2023 November 10; in original form 2023 September 12

## ABSTRACT

New photometry, including TESS data, have been combined with recent spectroscopic observations of the Orion Ib pulsating triple-star system VV Ori. This yields a revised set of absolute parameters with increased precision. Two different programs were utilized for the light curve analysis, with results in predictably close agreement. The agreement promotes confidence in the analysis procedures. The spectra were analysed using the FDBINARY program. The main parameters are as follows:  $M_1 = 11.6 \pm 0.14$  and  $M_2 = 4.8 \pm 0.06$  ( $M_\odot$ ). We estimate an approximate mass of the wide companion as  $M_3 = 2.0 \pm 0.3 M_\odot$ . Similarly,  $R_1 = 5.11 \pm 0.03$ ,  $R_2 = 2.51 \pm 0.02$ ,  $R_3 = 1.8 \pm 0.1$  ( $R_\odot$ );  $T_{e1} = 26600 \pm 300$ ,  $T_{e2} = 16300 \pm 400$  and  $T_{e3} = 10000 \pm 1000$  (K). The close binary's orbital separation is  $a = 13.91$  ( $R_\odot$ ); its age is  $8 \pm 2$  (Myr) and its photometric distance is  $396 \pm 7$  pc. The primary's  $\beta$  Cep type oscillations support these properties and confirm our understanding of its evolutionary status. Examination of the well-defined  $\lambda 6678$  He I profiles reveals the primary to have a significantly low projected rotation: some 80% of the synchronous value. This can be explained on the basis of the precession of an unaligned spin axis. This proposal can resolve also observed variations of the apparent inclination and address other longer-term irregularities of the system reported in the literature. This topic invites further observations and follow-up theoretical study of the dynamics of this intriguing young multiple star.

**Key words:** stars: binaries (including multiple) close — stars: early type — stars: variable  $\beta$  Cep type — stars: individual VV Ori

## 1 INTRODUCTION

VV Ori is a very bright ( $V \sim 5.4$ ,  $M_V \sim -2.8$  mag) and well-known eclipsing binary in the Belt, or  $\epsilon$  Ori, grouping of the Orion Ib association (Blaauw 1964; Wright 2020). Superficially, it resembles the system V Pup, with its period of  $\sim 1.5$  d and B1 + B3-5 type components (cf. Budding et al. 2021). However, numerous studies of the close pair in VV Ori have found a detached arrangement of young early-type main-sequence stars (cf. Fig 1), unlike the semi-detached configuration of V Pup. As the binary's orbital plane is close to

the line of sight, a succession of complete (or nearly so) eclipses is observed, allowing confidence about the determination of fitting function parameters including those relating to the distribution of brightness over the stellar surfaces.

Massive young stars like those in VV Ori are frequently found in groups of multiple star systems (Sana et al. 2012). Such star formation regions are thought to have an important role in determining the long-term behaviour of galaxies (Langer 2012; Zucker et al. 2022). A striking recent discovery about VV Ori, enabled by the long duration and high quality of TESS photometry (Ricker et al. 2014), is the existence of low-level  $\beta$  Cep type pulsations that may be associated with the primary star (Southworth et al. 2021).

\* Corresponding author: taylorssouthworth@gmail.com

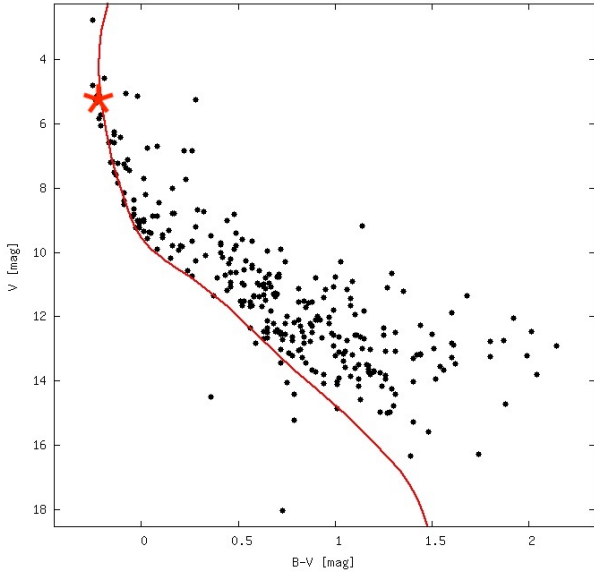


**Figure 1.** WEBDA colour-magnitude diagram based on the data of [Warren & Hesser \(1977\)](#). The Padova isochrone for  $\log(\text{age}) = 6.78$  y is shown with solar composition, reddening  $E(B - V) = 0.05$  and distance modulus 8.16. VV Ori is marked by a red coloured star.

It is well known that essential properties of stars can be determined from combining the analysis of photometric data with spectroscopic data — the ‘eclipse method’. We follow that approach for VV Ori. This has been more recently enhanced by the understanding of stellar pulsational behaviour, or asteroseismology ([Aerts et al. 2010](#); [Murphy 2018](#), [Bowman 2020](#)). A decomposition of the pulsations into constituent oscillation modes will furnish direct information on the stellar structure, particularly if constraints are imposed by membership of a co-evolutionary group of nearby stars ([Lampens 2006](#)).

With regard to early (B type) stellar pulsators, those of the  $\beta$  Cep ([Lesh 1978](#)) and slowly-pulsating (SPB) kinds ([Waelkens 1991](#)) are well known.  $\beta$  Cep variables show low-order gravity (g) and pressure (p) oscillation modes, with typical brightness variations of order 0.1 mag. They are associated with pulsation periods in the range 2 to 6 hr ([Stankov & Handler 2005](#)) and masses of around 8 to 15  $M_{\odot}$ . SPB pulsations have quite longer periods, generally a few days, and are found in the lower mass range of 3 to 9  $M_{\odot}$ . The variability is believed to result from high-order g-modes. More recent space-based observations, however, have uncovered both p- and g-type low-amplitude pulsations in many massive stars outside the foregoing ranges ([Pedersen et al. 2019](#); [Bursiens et al. 2020](#)).

Combining regular light and radial velocity (RV) curve analyses with asteroseismology, especially with recently increased data accuracy, permits stellar masses and radii to be more confidently specified ([Ratajczak et al. 2017](#); [Southworth et al. 2020, 2021](#); [Salmon et al. 2022](#)). That being said, stellar oscillations in massive eclipsing binaries have only been definitely established in relatively few cases so far (e.g., [Clausen 1996](#), [Southworth & Bowman 2022](#), [Erdem et al. 2022](#)). Stellar structural parameters may also be checked from eccentric close binary systems through non-Keplerian (apsidal) motion that relates to the scale of their proximity effects ([Sterne 1939](#); [Russell 1942](#); [Kopal 1959](#)). For more recent discussion, see also [Welsh et al. \(2011\)](#); [Hambleton et al. \(2013\)](#); [Feiden \(2015\)](#);

[Bowman et al. \(2019\)](#); [Handler et al. \(2020\)](#); [Kurtz et al. \(2020\)](#) and [Fuller et al. \(2020\)](#). A review of the use of space-based photometry for binary star science can be found in [Southworth \(2021\)](#).

VV Ori contains components of spectral types B1 V and mid-B V in an essentially circular orbit of period 1.485 d. Its eclipsing nature was discovered in 1903 ([Barr 1905](#)). The early history of its study was summarised by [Wood \(1946\)](#) and [Duerbeck \(1975\)](#). Two of the more recent published investigations of the system parameters are those of [Sarma & Vivekananda \(1995\)](#) and [Terrell et al. \(2007\)](#).

Multiplicity, beyond the two eclipsing stars, has been discussed in a number of studies over the years. Excess scatter in early RV data led to cautious suggestions of a third body with an orbital period of  $\sim 120$  d ([Daniel 1915](#); [Struve & Luyten 1949](#)), a proposal that has been disfavoured in later papers ([Terrell et al. 2007](#), [Van Hamme & Wilson 2007](#)). These latter papers cast doubt on the evidence for a close third body, at least regarding the RV analyses, though various photometric studies ([Budding & Najim 1980](#); [Chambliss 1983](#); [Van Hamme & Wilson 2007](#)) admitted a small third light contribution. However, [Horch et al. \(2017\)](#) have resolved a companion at an angular separation of 0.23 arcsec using speckle interferometry. The magnitude differences between this companion and the binary system are 3.88 mag at 692 nm and 3.43 mag at 880 nm. Applying a linear photometric gradient approximation ([Golay 1974](#)) would yield a magnitude difference of about 4.45 in the V range, or about 0.017 of the system’s light, which is essentially the same value found by [Chambliss \(1983\)](#). At a distance of  $441 \pm 22$  pc ([Gaia Collaboration et al. 2023](#)), the separation corresponds to a projected distance of  $\sim 87$  au, and thus a minimum orbital period of around 200 yr. This resolved companion cannot, therefore, be directly responsible for the putative 120 d orbital variations.

Recently, [Southworth et al. \(2021\)](#) noted that the succession of well-observed minima, over the years, has shown a transition between complete and partial eclipses. This can be associated with a systematic variation of the apparent inclination of the binary orbit to the line of sight. That there may be some variations of shorter period than that of the wide orbit is thus still an open question.

A consensus from radial velocity studies ([Daniel 1915](#); [Struve & Luyten 1949](#); [Beltrami & Galeotti 1969](#); [Duerbeck 1975](#); and [Popper 1993](#)) presented the system as mostly single-lined, though [Beltrami & Galeotti \(1969\)](#) were able to model blended line profiles to derive a velocity separation and thence a mass ratio of  $\sim 0.45$ ; similar to that of [Duerbeck \(1975\)](#).

In this study, we bring new evidence to bear on outstanding uncertainties about the system, regarded as important for fixing the properties of massive early-type stars ([Eaton 1975](#); [Popper 1993](#); [Terrell et al. 2007](#); [Van Hamme & Wilson 2007](#); [Southworth et al. 2021](#)). We examine new high quality photometry from the TESS satellite, and high-dispersion spectroscopy from the FIES spectrograph of the 2.56-m Nordic Optical Telescope, Tenerife, Spain; as well as the HERCULES spectrograph of the University of Canterbury Mt John Observatory, New Zealand. These new data yield important revisions in the physical properties of the component stars. We use up-to-date analytical tools to bear on the data analysis, and check on evolutionary models, keeping in mind additional evidence relating to the Orion OB 1b membership and the degree of multiplicity of VV Ori.

## 2 PHOTOMETRY

Table 1 presents a summary of the main parameters derived in previous photometric studies of VV Ori light curves (LCs) at visual (V)

wavelengths. Standard notation is used, i.e.  $L_n$  for fractional luminosities (where  $n$  indicates a given star in the system),  $r_n$  for relative radii,  $i$  for the orbital inclination, and  $u_n$  for linear limb-darkening coefficients. The sources of these parameters are as follows: Du-75 = Duerbeck (1975); Na-81 = Budding & Najim (1980); Ch-84 = Chambliss (1984); Sa-95 = Sarma & Vivekananda (1995); Te-07 = Terrell et al. (2007); So-21 = Southworth et al. (2021). Some variations of parameter values can be noticed across Table 1, but these are generally in keeping with the listed uncertainties. This table is not intended to be exhaustive, but it gives an impression of reference quantities derived from data analysis over the last several decades, keeping in mind concomitant increases of data accuracy.

Further multi-colour photometry of VV Orionis (see Table 2) was carried out over ten nights between December 2018 and February 2019 from the Congarinni Observatory, NSW, Australia ( $152^\circ 52' \text{ E}$ ,  $30^\circ 44' \text{ S}$ , 20 metres above mean sea level). Images were captured with an ATIK<sup>TM</sup> One 6.0 CCD camera equipped with Johnson-Cousins BVR filters attached to an 80mm f6 refractor, which, given the brightness of the stars, was stopped down to 50mm aperture. MaxIm DL<sup>TM</sup> software was used for image handling, calibration and aperture photometry. HD 36779 was used as the main comparison star. Its magnitude and colours were determined as  $V = 6.223$ ,  $B - V = -0.165$  and  $V - R = -0.067$ , in close agreement with the Johnson 11-colour catalogue (Ducati 2002). The derived light curves are shown in Fig. 2. Optimal parameters from WINFITTER modelling (cf. Rhodes 2022) are given in Table 3. Using the results given in Table 2 as a guide, we derived BVR magnitudes of the three identified photometric components of VV Ori as: 5.23, 8.00, 9.95 (B); 5.41, 8.02, 9.79 (V); 5.65, 8.09, 9.61 (R). Taking into account local variations of the mean reddening ( $\sim 0.09$ , according to Warren & Hesser, 1978) and errors of measurement, these figures are in fair accord with the assigned early and mid-B main sequence types for the close pair attended by a cooler, A-F type, companion.

## 2.1 Light curve analysis

We first sought to match the form of the light curve with the well-known Wilson-Devinney (WD) code (Wilson & Devinney 1972; Wilson 1979). We used the 2004 version of the code (Wilson & van Hamme 2004) implemented using the JKTD wrapper (Southworth et al. 2011). This code adopts Roche model geometry for the calculation of the shapes of binary stars (cf. Kopal 1959; ch. 3), although it becomes computationally expensive to perform on the original complete set of TESS observations. We therefore took the data from sector 6, converted them to orbital phase, and averaged them into 400 equally-spaced phase bins.

These data were then fitted using WD to obtain the simplest initial model that matched them well. This, our default solution, was obtained by fitting the following model parameters: surface potentials of the two stars, orbital inclination, phase of the primary mid-eclipse, and light contributions of both eclipsing stars together with a possible third light. The third light is expressed as a fraction of the total brightness of the system at phase 0.25. The light contributions from the two stars are expressed in the WD code on a different flux scale, and add to  $4\pi$  minus the third light for zero differential magnitude. The fitting was performed in mode 0 (see Table 4), where the effective temperature ( $T_e$ ) values of the two stars are fixed and their light contributions matched directly. We therefore fixed the  $T_e$  values and mass ratio at the adopted spectroscopic values, presented in Section 3, and assumed a circular orbit. We also assumed, for the present purpose, synchronous rotation, as well as albedo parameters and gravity darkening exponents set to

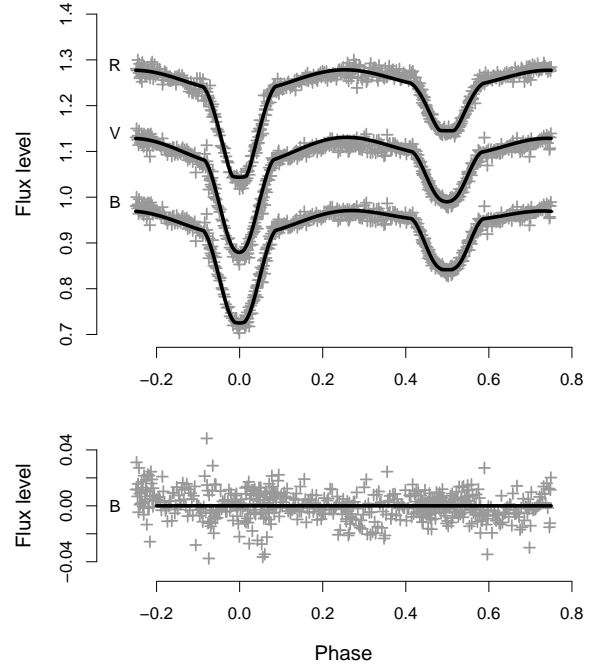


**Figure 2.** WINFITTER model fitted to recent BVR light curves from the Congarinni Observatory. The V and R light curves have been vertically offset by 0.15 and 0.30 to allow presentation on a single chart.

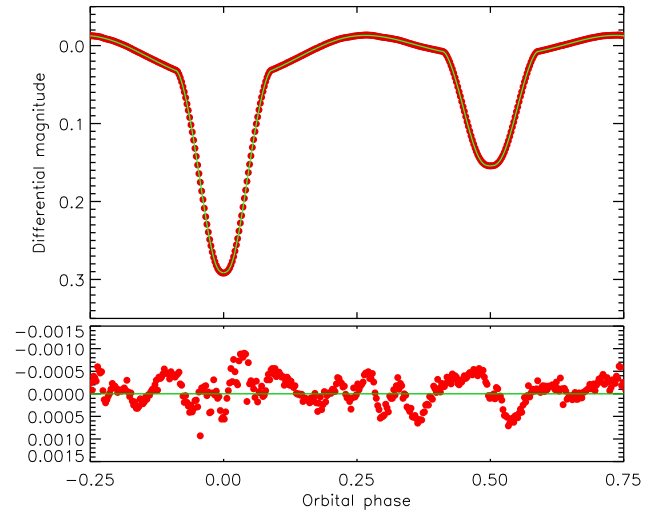


**Figure 3.** The adopted optimal WD model (green line) to the TESS sector 6 phase-binned light curve of VV Ori (red filled circles). The residuals of the fit are plotted in the lower panel using a greatly enlarged y-axis to bring out the detail.

unity. The limb darkening (LD) effect was accounted for using a logarithmic law with one coefficient adjustable and the other fixed, for both stars. Maximum numerical precision was used, by setting the quantities N1, N2, N1L and N2L to 60. For the effective wavelength of observation, the Cousins R band was adopted as it is the closest available approximation to the TESS passband. The ‘simple’ option for the reflection effect was chosen.

With these settings in place, we were able to obtain a satisfac-

**Table 1.** Reference parameters for historic photometric model fits.

Parameter	Du-75	Na-80	Ch-84	Sa-95	Te-07	So-21
$\lambda$ nm	540	425	530	530	(530)	TESS
$M_2/M_1$	0.45	0.45	0.42	0.42	0.38	0.376
$L_1$	$0.878 \pm 0.06$	$0.926 \pm 0.09$	$0.891 \pm 0.10$	$0.878 \pm 0.01$	$0.908 \pm 0.09$	$0.892 \pm 0.07$
$L_2$	$0.122 \pm 0.04$	$0.069 \pm 0.03$	$0.092 \pm 0.05$	$0.122 \pm 0.01$	$0.098 \pm 0.05$	$0.103 \pm 0.005$
$L_3$	$0.000 \pm 0.06$	$0.005 \pm 0.03$	$0.017 \pm 0.11$	$0.00 \pm 0.01$	$0.00 \pm 0.07$	$0.005 \pm 0.07$
$r_1$	$0.366 \pm 0.006$	$0.371 \pm 0.01$	$0.363 \pm 0.02$	$0.378 \pm 0.02$	$0.369 \pm 0.005$	$0.372 \pm 0.001$
$r_2$	$0.180 \pm 0.01$	$0.168 \pm 0.03$	$0.176 \pm 0.05$	$0.179 \pm 0.05$	$0.179 \pm 0.013$	$0.182 \pm 0.003$
$i$	$85.6 \pm 1.0$	$85.8 \pm 1$	$85.6 \pm 2$	$86.1 \pm 5$	$85.9 \pm 0.5$	$78.3 \pm 0.5$
$T_h$ (K)	25000	25000	25000	25000	26199	26200
$T_c$ (K)	15000	16000	15700	15500	16073	16100
$u_1$	0.07	0.37	0.28	0.33	–	0.63 (bol)
$u_2$	0.45	0.45	0.32	0.37	–	0.71 (bol)

**Table 2.** Summary of Congarinni BVR photometry of VV Ori, along with uncertainties, given as standard deviations.

Date	Phase	V	stdev	B – V	stdev	V – R	stdev
19 01 26	0.0	5.627	0.034	–0.140	0.042	–0.113	0.046
18 12 25	0.5	5.465	0.017	–0.157	0.024	–0.114	0.021
18 12 28	0.5	5.467	0.016	–0.166	0.021	–0.113	0.023
18 12 29	0.25	5.308	0.022	–0.157	0.029	–0.114	0.034
19 01 25	0.25	5.314	0.022	–0.157	0.032	–0.104	0.035
18 12 29	0.75	5.281	0.020	–0.158	0.028	–0.125	0.021

**Table 3.** Parameters for model fits to the BVR photometry shown in Fig 2. Adopted parameters are listed below the 3rd row horizontal line. The geometric elements  $r_1$ ,  $r_2$  and  $i$ , are weighted averages from initial fittings at the separate wavelengths. The value of  $L_3$  in the B filter, being expectably less than its uncertainty as an optimal fitting result, is here a fixed hyperparameter.

Parameter	B	V	R
$L_1$	$0.926 \pm 0.012$	$0.901 \pm 0.013$	$0.894 \pm 0.013$
$L_2$	$0.072 \pm 0.003$	$0.082 \pm 0.003$	$0.085 \pm 0.003$
$L_3$	0.012	$0.016 \pm 0.014$	$0.021 \pm 0.013$
$r_1$ (mean)	$0.359 \pm 0.008$		
$r_2$ (mean)	$0.171 \pm 0.004$		
$i$ (deg, mean)	$80.0 \pm 0.8$		
$M_2/M_1$	0.42		
$T_h$ (K)	26600		
$T_c$ (K)	16250		
$u_1$	0.28	0.25	0.21
$u_2$	0.29	0.29	0.24
$\chi^2/\nu$	1.01	1.05	0.90
$\Delta I$	0.014	0.012	0.010

tory fit to the phase-binned data as shown in Fig. 3. The residuals are shown on a larger scale to demonstrate the presence of structure remaining in the phase-binned data. Whilst the differences between observed and calculated LCs are relatively small (an r.m.s. of 0.3 mmag), the remaining pulsational signature means the residuals are dominated by red noise. Using fitting procedures that allowed for orbital eccentricity, we conclude that the quantity  $e \cos \omega$ , where  $e$  is the eccentricity and  $\omega$  the longitude of periastron, must be

**Table 4.** Summary of the parameters for the WD fittings of the TESS sector 6, phase-binned light curve of VV Ori. Detailed descriptions of the control parameters can be found in the WD code user guide (Wilson & van Hamme 2004). The uncertainties have been determined via comparisons through a wide range of model fits.

Parameter	WD2004 name	Value
<i>Control &amp; fixed parameters:</i>		
WD2004 operation mode	MODE	0
Treatment of reflection	MREF	1
Number of reflections	NREF	1
LD law	LD	2 (logarithmic)
Numerical grid size (normal)	N1, N2	60
Numerical grid size (coarse)	N1L, N2L	60
<i>Fixed parameters:</i>		
Mass ratio	RM	0.418
Orbital eccentricity	E	0.0
$T_e$ of primary (K)	TAVH	26,660
$T_e$ of secondary (K)	TAVH	16,250
Bolometric albedos	ALB1, ALB2	1.0, 1.0
Rotation rates	F1, F2	1.0, 1.0
Gravity darkening	GR1, GR2	1.0, 1.0
Logarithmic LD coefficients	Y1A, Y2A	0.217, 0.205
<i>Fitted parameters:</i>		
Primary potential	PHSV	$3.220 \pm 0.026$
Secondary potential	PHSV	$3.637 \pm 0.023$
Orbital inclination (deg)	XINCL	$79.77 \pm 0.19$
Primary light contribution	HLUM	$10.48 \pm 0.10$
Secondary light contribution	CLUM	$1.215 \pm 0.012$
Third light	EL3	$0.071 \pm 0.008$
Primary linear LD coefficient	X1A	$0.359 \pm 0.049$
Secondary linear LD coefficient	X2A	$0.22 \pm 0.15$
Fractional radius of primary		$0.3656 \pm 0.0019$
Fractional radius of secondary		$0.1794 \pm 0.0015$

smaller than 0.001. A summary of the fitted and fixed parameters is given in Table 4. The fractional stellar radii specified in Table 4 are volume-equivalent values. Table 3-2 in Kopal's (1959) book shows these radii to be one or two percent larger than the corresponding unperturbed radii ( $r_0$ ) at the same mass ratio.

Determination of the uncertainties of the fitted parameters is not trivial. We follow the approach of Southworth (2020) on this.

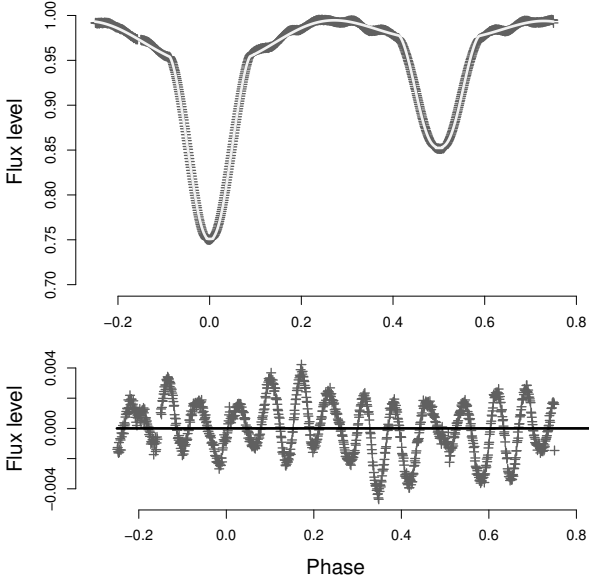


**Figure 4.** The upper panel presents an optimal model LC to normalized SAP flux measures from TESS for the orbit 13 of Sector 6, TBJD 1487.38930345 – 1488.87467768, 1070 data points were taken from the original source with no binning. The lower panel reveals the  $\beta$  Cep type behaviour in the residuals.

The uncertainties derive almost entirely from the model limitations, even taking into account the residual pulsation signature, because the precision of the data is extremely high, showing up systematic effects that are not in the model. We therefore ran WD with selected differences in parameter values to determine their effects on the resulting fits, as follows:

- changing the mass ratio by the uncertainty in the spectroscopic value;
- fixing  $e \sin \omega = 0.005$ , instead of assuming a circular orbit;
- decreasing the rotation parameters for the stars by 10%;
- changing the albedos by 10%;
- changing the gravity darkening exponents by 10%;
- lowering the  $N_1, N_2$  values from 60 to 55 in steps of 1;
- fitting for  $T_c$  in mode 2, instead of fitting for HLUM and CLUM in mode 0;
- using the more detailed reflection model;
- specifying the square-root instead of the logarithmic limb darkening law
- using the Cousins  $I$  filter for the TESS pass-band;
- fixing third light to be zero;
- changing the number of phase bins from 400, to 300 or 500.

The net result of these tests was a compilation of values for the fitted parameters; each group associated with a different model run. We rejected all runs where the fit was significantly worse (more than 0.35 mmag r.m.s. in the residuals), and added all the parameter differences in quadrature to determine the uncertainty for each fitted parameter. These are given in Table 4. The largest contributions to these uncertainties were found to come from the effects of the adopted rotation, albedo and eccentricity parameters. The derived uncertainty percentages are nonetheless still small, and the fitted parameters have highly consistent values.

For an independent assessment of the LC we used the program WinFitter (WF), discussed in Budding & Demircan (2022) chapter

**Table 5.** Optimal WinFitter parametrization of TESS photometry from Sectors 6 and 32, modelling the entire sectors. The data-sets were phased by the orbital period, thus averaging out the pulsations. The column titled ‘Figure 4’ lists the parameter estimates for the data period plotted in Figure 4. The mass ratio, stellar temperatures, and limb darkenings are held constant across these fits.

Parameter	Sector 6	Sector 32	Figure 4
$L_1$	$0.847 \pm 0.010$	$0.875 \pm 0.006$	$0.860 \pm 0.013$
$L_2$	$0.098 \pm 0.003$	$0.096 \pm 0.002$	$0.100 \pm 0.004$
$L_3$	$0.055 \pm 0.005$	$0.008 \pm 0.003$	$0.040 \pm 0.005$
$r_1$	$0.371 \pm 0.002$	$0.370 \pm 0.002$	$0.368 \pm 0.002$
$r_2$	$0.183 \pm 0.003$	$0.184 \pm 0.003$	$0.181 \pm 0.001$
$i$ (deg)	$78.2 \pm 0.4$	$78.0 \pm 0.4$	$79.0 \pm 0.5$
$M_2/M_1$		0.48	
$T_h$ (K)		26600	
$T_c$ (K)		16250	
$u_1$		0.18	
$u_2$		0.20	
$\chi^2/\nu$	1.14	0.97	0.90
$\Delta I$	0.0013	0.002	0.0025

7. The algebraic form of its fitting function means that parameter space can be searched rapidly and thoroughly using relatively large data-sets. An example of a LC from TESS Sector 6 is shown in Fig. 4 together with an optimal WF model. The residuals are shown in the lower panel where the  $\beta$  Cep oscillations of the primary component are clearly evident. The adopted light elements for this data set were:

$$\text{Min I} = \text{TBJD}1487.389303 + 1.48537742E.$$

LCs from both Sectors 6 and 32 were collected together, phased and binned using this ephemeris. The Sector 6 data were binned with a reduction factor of 14:1 down from 14,847 original data points, while Sector 32 data were binned with the ratio 17:1, from the 17,917 source data. Numerous optimal fitting experiments were performed on these reduced data-sets. Starting values were guided by historic findings. The finally adopted parameter sets are given in Table 5, and are in reasonable agreement with the WD model parameters. The separately derived main geometric elements ( $r_1, r_2, i$ ) of the WD and WF fittings to the TESS data-sets are within the uncertainty estimates of each other. They concur that the TESS data point to a distinctly lower inclination than the values cited in Table 1.

## 2.2 Fitting function with unaligned axes

It was mentioned above that Southworth et al. (2021) discussed visible LC effects associated with an apparent variation of the inclination parameter. The precession of a spin axis that is unaligned to that of the orbit is feasible for a young multiple system in a process of angular momentum evolution, and, since the flux from the system is dominated by the primary star, such effects would be mainly associated with the behaviour of that star. In this section we check on the scale of relevant effects and how the WF fitting function may address this topic.

In general, the matching of a theoretical model to a photometric data set (LC) is achieved by optimizing the agreement of a fitting function  $I(\phi; a_i)$ , where  $\phi$  is the orbital phase and  $a_i$  are a set of parameters whose adjustment is implied by the optimization

process. This fitting function can be set in the form:

$$l(\phi) = \int_{A_1} J_1 dA_1 + \int_{A_2} J_2 dA_2 - \int_{A_e} J_e dA_e \quad (1)$$

where the suffix 1 refers to the ‘primary’ object, with higher surface temperature, say, having projected surface area  $A_1$ , while suffix 2 denotes the secondary, projecting area  $A_2$  perpendicular to the line of sight. The received flux scales linearly with the integrated locally projected flux  $J$  from either source. The suffix  $e$  relates to an eclipse: the relevant term is zero when there is no eclipse and maximizes during complete eclipse phases. Eclipses of the secondary star are covered by the same form, but with the eclipsing and eclipsed roles reversed,  $J_e$  being suitably re-assigned.

Eqn 1 is reducible to a relatively simple form in the ‘spherical model’ (cf. [Russell & Shapley 1912](#)). This reduction suggests that modelling can be developed to cater for more realistic situations using the Taylor expansion

$$l(\phi) = l_0(\phi) + \Delta l_{A1}(\phi) + \Delta l_{A2}(\phi) - \Delta l_{Ae}(\phi), \quad (2)$$

where  $l_0(\phi)$  in Eqn 2 would be normalized so that the sum of the first two integrals, in the unperturbed, uneclipsed situation, is unity. In this case, the first term becomes the primary’s fractional luminosity  $L_1$ , the second, correspondingly,  $L_2$ .

We can adopt, without loss of generality, that suffix 1 refers to the star about to be eclipsed and the zero order LC equation becomes

$$l_0(\phi) = 1 - \alpha\{u_1, k, d(r_1, i, \phi)\}L_1, \quad (3)$$

where  $\alpha$  is Russell’s ([1912a](#); [1912b](#)) light loss function, depending here on the re-normalized separation  $d = \delta/r_1$ ;  $\delta$  being the separation of the two star centres in units of the mean orbital radius on the tangential sky plane, given by

$$\delta^2 = \sin^2 \phi \sin^2 i + \cos^2 i. \quad (4)$$

Other parameters include the ratio of radii  $r_2/r_1$ , written as  $k$  in Eqn(3), and a limb-darkening coefficient  $u_1$ .

For a more realistic model we should evaluate the effects of tidal and rotational perturbations of the photosphere, associated with the proximity of the two stars, at given phases, as well as the ‘reflection’ effects that result from their mutual irradiation. Calculating the surface distortion involves the radial displacements in the key directions of the line of centres and the axis of rotation. Local areal projections for any viewing angle are then resolved into their components in the observer’s frame of reference.

Both WD and WF converge to the same approximation for the first order surface perturbation given as

$$\frac{\Delta' r}{r_0} = q \sum_{j=2}^4 r_0^{j+1} (1 + 2k_j) P_j(\lambda) + nr_o^3 (1 - \nu^2) \quad (5)$$

where  $r$  is the local stellar radius expressed as a fraction of the orbital separation of the components with mean value  $r_0$ , and  $k_j$  are the well-known structural constants reflecting the distribution of matter through the star.  $\lambda$  is the direction cosine of the angle between the radius vector  $\hat{r}$  and the line of centres, and  $\nu$  is the direction cosine of the angle between  $\hat{r}$  and the rotation axis. The coefficients  $k_j$  can be taken from suitable stellar models, e.g. [Inlek et al. \(2017\)](#), or set to zero in the Roche model (cf. Eqns 1-11 in Ch.1, and 2-6 in Ch. 3 of [Kopal, 1959](#)).

With the surface perturbations as serial harmonic functions, they are seen (Eqn 5) to start with terms of order  $r^3$ , so by the time we reach terms of order  $r^6$  the gravitational interaction of

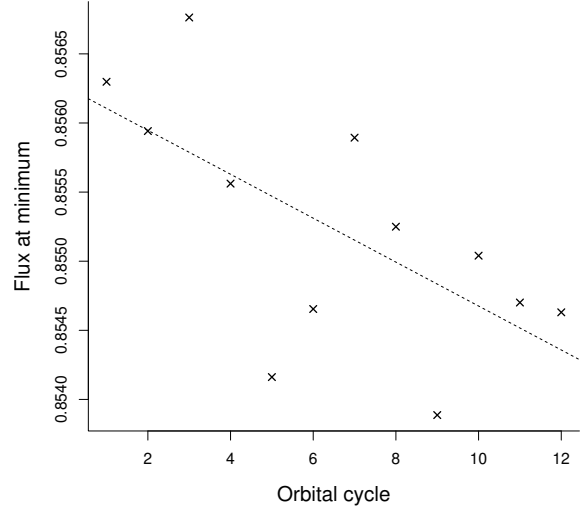


**Figure 5.** A trend across a flux interval of several mmag can be seen in the succession of TESS monitorings of secondary minima in the Sector 6 data.

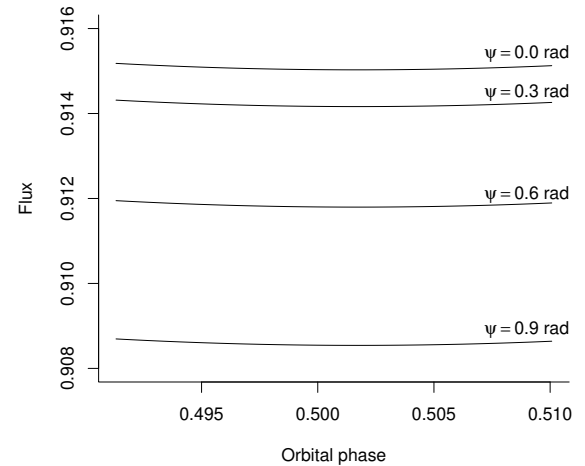


**Figure 6.** The effects of varying the precession angle of the primary star’s spin axis, at a 20 deg obliquity, on the relative flux during secondary minimum.

tides on tides would be taken into account. WF analysis, in which the mutual effect of perturbations on perturbations is neglected, therefore proceeds up to and including terms of order  $r^5$ . This implies three separate tidal terms in the fitting function.

Rotation with a constant angular velocity, as is usually assumed, requires only one source term. However, location of the rotation axis with respect to the orbit will, in general, involve two additional angular parameters:  $\epsilon$  the obliquity and  $\psi$  the precession angle. In the case of aligned rotation and orbit axes, the surface distortions due to rotation, as they appear to a remote observer, involve integrals factored by orientation-dependent direction cosines. These reduce down to the independent cosine of the angle between the line of sight and the rotation axis  $n_0$ . This becomes replaced, in the unaligned case, by  $n'_0$ , where

$$n'_0 = n_0 \cos \epsilon + \sin i \sin \epsilon \cos \psi \quad (6)$$

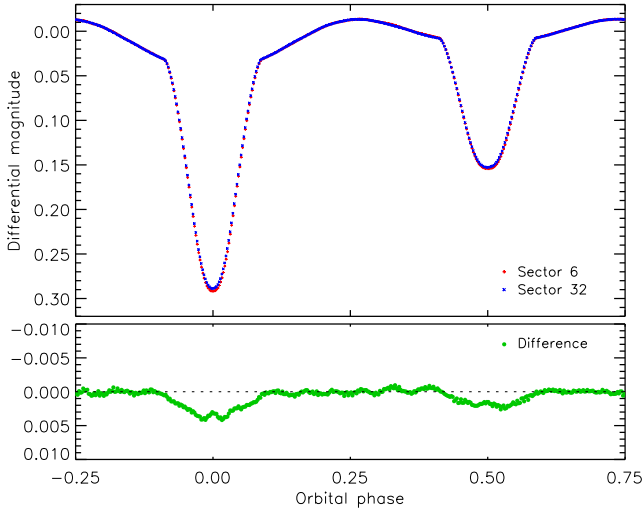


**Figure 7.** Phase-binned versions of sectors 6 and 32 TESS observations (top) and their difference on a magnified scale (bottom).

(cf. Eqn (1.13) of [Budding & Demircan 2022](#)).

Fig. 5 plots the measured depths of the secondary minima over a succession of LCs from TESS sector 6 with mean epoch TJD 1477.5973. This comes from averaging the values of 13 individual flux measures — at phase 0.5 and the 6 points on either side. A trend of order 2 mmag becomes apparent over the 18 day time interval. LC modelling of the partial, but near total, secondary eclipse shows that this would necessitate a change of inclination significantly greater than the  $\sim 0.01^\circ$  (for 18 d) considered by [Southworth et al. \(2021\)](#) after inspection of historic LCs. However, the residuals presented in Fig. 4 allow an expectation of point-to-point variations in Fig. 5 of several mmag, so this apparent short-term trend is not separable from effects *not* due to inclination changes. On the other hand, LC modelling shows that variations of several mmag in the central depth of the secondary minimum would result from changes of the apparent inclination, i.e.  $\arccos(i'_0)$ , of order  $1^\circ$ . Fig. 6 shows that this could be accounted for by precessional movement of order  $\sim 10^\circ$  on a feasible timescale of  $\sim 10$  yr.

A further series of TESS LCs with mean epoch TJD 2186.0373, i.e. 708.44 d later, were collected in sector 32. Unfortunately, this nearly 2 yr time baseline produces only a  $0.4^\circ$  shift in the inclination at the rate presented by [Southworth et al.](#), so comparable to the uncertainty in the estimated inclination values of Tables 4 and 5. The mean relative fluxes at mid-secondary minimum from the two sectors are  $0.8549 \pm 0.0015$  and  $0.8551 \pm 0.0014$ , which does not yet provide convincing support for a secular change in the relative depth of the secondary minimum over the two years separating the two TESS sectors involved.

### 2.3 Evaluation of changes between TESS sectors

The hypothesis of orbital evolution associated with a third body, or some other cause, leads naturally to the suggestion that the light curve may change between the two TESS sectors. [Southworth et al. \(2021\)](#) found a change in orbital inclination which in turn may change the eclipse depths. We therefore searched for these effects.

We first fitted the two TESS sectors simultaneously to obtain an orbital ephemeris which precisely matched these datasets without influence from other data. We then phase-binned each TESS sector into 400 bins (as done above). A plot of these sectors and the

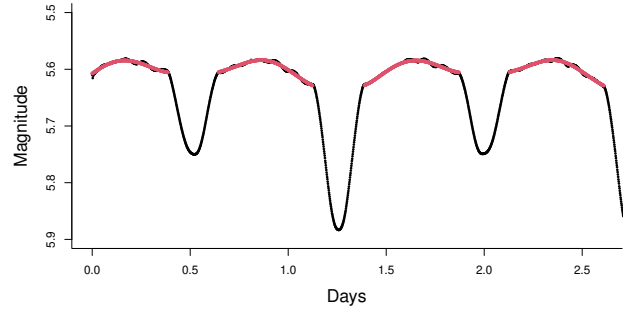


**Figure 8.** The first 2.5 days of TESS Simple Aperture Photometry (SAP) from Sector 32. Out-of-eclipse regions used for frequency analysis are shown in red.

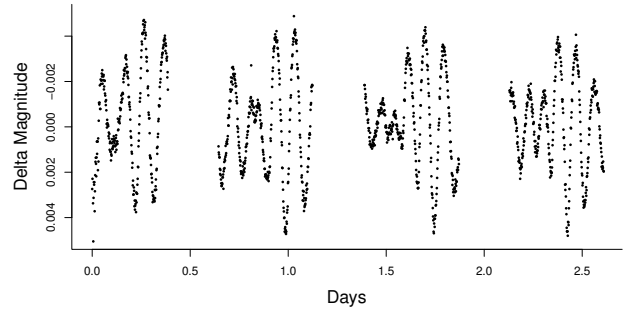


**Figure 9.** Residual pulsations in the inter-minimum phases after removing the eclipsing binary LC.

difference between them can be found in Fig. 7. A decrease in the eclipse depths is clear.

We then fitted both datasets using the Wilson-Devinney code (see Section 2.1). For each fit we adopted one approach to modelling the data-sets, and analysed them separately. We performed a range of fits varying the numerical precision of the code, the treatment of rotation, albedo and limb darkening. The differences in orbital inclination across all fits averaged at close to  $0.17^\circ$  (mean) with a standard deviation of  $0.08^\circ$ . We therefore find a change in inclination to a significance level of  $2\sigma$  over a time period of 706 d. The LC clearly changes, but we are not yet able to quantify this with sufficient statistical significance. It is unfortunate that no further observations of VV Ori by TESS are currently scheduled.

An alternative explanation of the change in eclipse depth is imperfections in the data reduction. An obvious possibility is an error in the background subtraction which would shift the light curve up or down by a fixed amount of flux. In this case we would expect to see the difference between the TESS sectors (Fig. 7) appear as a scaled-down version of the light curve. That is not the case: the differences between sectors occur only during the eclipses. This supports the possibility of changing apparent inclination in the eclipsing pair in the VV Ori system.

### 2.4 Frequency analysis of TESS data

[Southworth et al. \(2021\)](#) performed a frequency analysis of pulsations in the Sector 6 TESS photometry of VV Ori, recorded in

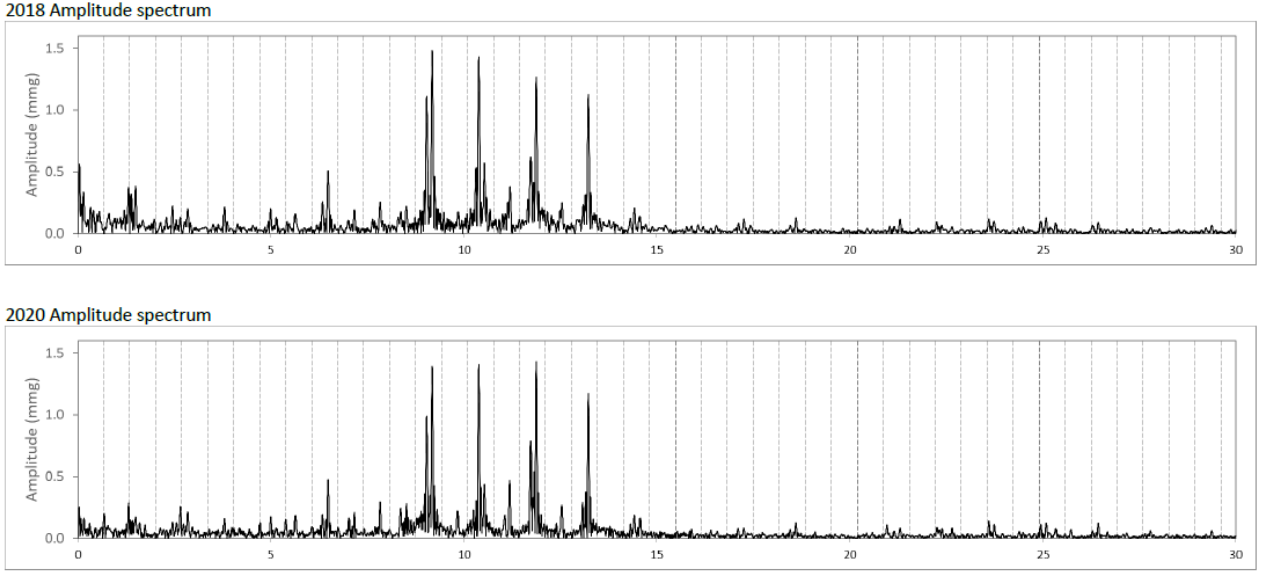


**Figure 10.** Frequency spectra of VV Ori using `PERIOD04` on the residuals from the 2018 and 2020 binary LC fittings to the TESS datasets.

2018-19. They found 51 significant frequency components between  $1.4$  and  $27.8 \text{ d}^{-1}$ , with two dominant pulsation modes ( $\nu_1 = 9.1766 \pm 0.0001$  and  $\nu_2 = 9.0324 \pm 0.0002 \text{ d}^{-1}$ ). There were also several independent g-mode frequencies below  $3 \text{ d}^{-1}$ . These components were attributed to  $\beta$  Cep oscillations of the primary and SPB variations of the secondary, respectively.

Here, we have analysed Sector 32 pulsations recorded in 2020, using a different approach to removing the close binary contribution to the LC. Fig. 8 shows part of the simple aperture photometry (SAP) LC. For clarity, only the first 2.5 days are presented; however, all 27 days' data were analysed. Only the out-of-eclipse observations (shown in red) were used in the frequency analysis, in order to avoid complications to the pre-whitening operation arising from eclipse effects. The proximity effects were removed empirically, by fitting 6th-order polynomials to the out-of-eclipse sections of the phased LCs. The maxima before and after primary eclipses were fitted separately. Residual pulsations after subtracting the polynomial models are shown in Fig. 9. We used the same methodology to analyse the Sector 6 data, allowing direct comparison with the results from Southworth et al. (2021).

Frequency analysis of residual pulsations was performed using `PERIOD04` software (Lenz & Breger 2004). Iterative pre-whitening identified 60 significant frequencies with amplitude signal-to-noise  $> 4$ . The frequencies, amplitudes, and phases are listed in Table A1. Fig. 10 presents the frequency spectra based on the residuals from the LC fittings to the 2018 and 2020 data. General features of the Sectors 6 and 32 amplitude spectra are similar. The two dominant frequencies reported in Southworth et al. (2021) remain and with similar amplitudes. The frequencies we obtain are: (2018)  $9.17680 \pm 0.00007$  and  $9.03131 \pm 0.00016 \text{ d}^{-1}$ ; and (2020)  $9.17726 \pm 0.00007$  and  $9.03282 \pm 0.00017 \text{ d}^{-1}$ . The relative amplitudes of peaks between  $9$  and  $14 \text{ d}^{-1}$  are different, however, while the cited frequencies differ by more than their formal uncertainty estimates. This may be attributed to the different data extraction methods employed, but slight changes in the pulsation properties in the two years between the TESS observation sets cannot be ruled out in view of the low level of the formal errors.

### 3 SPECTROMETRY

Spectroscopic data examined in this study include observations made with the `HERCULES` spectrograph (Hearnshaw et al. 2002), using the 1m McLellan telescope at the University of Canterbury Mt John Observatory (UCMJO) ( $\sim 43^\circ 59'S$ ,  $174^\circ 27'E$ ) in New Zealand. Around 25 spectral images were obtained, distributed over the period 2010-15. These UCMJO observations provide somewhat incomplete coverage for the first half of the full cycle, but allow a consistent result. The data were collected with a  $4k \times 4k$  Spectral Instruments (SITE) camera (Skuljan 2004). Starlight from the telescope was passed to the spectrograph by a  $100 \mu\text{m}$  effective diameter fibre, corresponding to a theoretical resolution of  $\sim 40,000$ . Wavelength and relative flux calibration was performed using the latest version of the software package `HRSP` (Skuljan 2020) that outputs measurable data in `FITS` (Wells et al. 1981) formatted files. Fair weather exposures were usually for  $\sim 500$  seconds.

Some 45 clear orders (80 to 125) of the échelle were set up for inspection, using the software package `VSPeC` (Desnoux & Buil 2005)<sup>1</sup>. Useful spectra typically have a signal to noise ratio (S/N) of  $\sim 100$  in order 85. Given the high red-sensitivity of the SITE camera, this drops to  $\sim 50$  by order 125.

Table A2<sup>2</sup> lists individual lines, mainly of the primary, detected in this study. Apart from  $H_\alpha$  and  $H_\beta$ , the best defined line is probably the primary He I  $\lambda 6678$  line, where the corresponding weak secondary feature is also seen. A similar situation holds at He I  $\lambda 5875$ ; but the other He lines appear weaker and the secondary is not clearly distinguished at  $\lambda 5047$ . High excitation lines of C, N, O and Si are increasingly seen in the higher orders, though their S/N deteriorates and blending can be expected as the primary non-hydrogen lines are  $\sim 6-8 \text{ \AA}$  wide. The He II feature at  $\lambda 4686$ , together with the high-excitation lines, suggest the type may be a

<sup>1</sup> This is an MS-Windows<sup>TM</sup> based package that includes essential data-processing functions.

<sup>2</sup> Placed in the appendix on page 16 to avoid disrupting the flow of the paper.



**Table 6.** Radial velocity data of the components of VV Ori derived from the He I lines.

BJD 2450000+	Orbital phase	RV1 km s <sup>-1</sup>	RV2 km s <sup>-1</sup>
5539.9398	0.4272	-26.83	—
5539.9576	0.4391	-24.28	—
5544.8758	0.7502	164.45	-302.3
5544.8917	0.7609	163.44	-302.3
5544.9560	0.8040	146.60	-66.1
5545.0213	0.8482	134.39	-192.6
5549.9023	0.1342	-97.22	—
5798.2189	0.3083	-127.32	282.3
5798.2600	0.3360	-120.18	276.7
5798.2737	0.3452	-120.69	280.8
5875.9380	0.6311	157.24	-190.7
5875.9391	0.6318	133.34	-221.2
5875.9529	0.6411	142.01	-226.8
5875.9530	0.6411	157.22	-208.6
5876.0580	0.7119	181.71	-58.2
5876.0584	0.7121	153.74	-282.9
5876.0720	0.7213	181.67	-260.5
5876.0724	0.7216	159.35	-266.1
5880.0972	0.4312	-15.61	—
6255.1256	0.9114	75.7	—
6258.0204	0.8602	109.36	-231.9
6258.0690	0.8930	101.71	-236.0
6666.9080	0.1355	-95.60	282.5
6673.9112	0.8502	106.81	-240.0
6675.0142	0.5928	107.71	-187.0
6993.9697	0.3231	-194.65	202.7
7350.1629	0.1229	-99.01	261.9
7356.1382	0.1456	-109.98	268.8

bit earlier than the oft-cited B1. The interstellar Na II lines reported by Terrell et al. (2007) are confirmed and separated into two main concentrations separated by about 0.33 Å (~17 km s<sup>-1</sup>).

The UCMJO data on VV Ori were combined with a set of 45 high-resolution spectra taken in 2006 and 2007 with the FIES spectrograph at the Nordic Optical Telescope (NOT) at the Roque de los Muchachos Observatory, La Palma, Canarias, Spain. This facility has been reviewed by Telting et al. (2014). Although some disparities were encountered in combining the FIES and HERCULES data, the sharp interstellar sodium lines are quite prominent and useful for checking wavelength calibration. The greatest deviations show up in the last two spectra obtained with HERCULES. These images from Dec 2015 are separated by over a year from the main cluster of observations (Table 6). The FIES spectra form a more compact dataset, coming from two short observing runs in Nov 2006, and Oct 2007. In the context of possible secular changes in RV curves, it would be desirable to complete phase coverage over as short an interval as possible.

### 3.1 Spectral disentangling: determination of the orbital parameters

Spectral lines in high-mass binary systems, like VV Ori, are usually broadened by high rotational velocities and often become blended over the course of the orbital cycle. Therefore, direct RV measurements are probably uncertain. In such cases, even more modern cross-correlation function (CCF) techniques become ineffective.

Spectral disentangling (Simon & Sturm 1994; Hadrava 1995)

**Table 7.** The orbital parameters for VV Ori determined by spectral disentangling. The orbit is essentially circular, hence only the RV semi-amplitudes  $K_1$ , and  $K_2$  of the components are determined (see Fig 12). The derived values of the mass ratio,  $q$ , and masses of the components,  $M_1$ , and  $M_2$  multiplied by  $\sin^3 i$ , are given.

Parameter	Value	Uncertainty
$K_1$ km s <sup>-1</sup>	137.20	± 0.59
$K_2$ km s <sup>-1</sup>	328.58	± 1.56
$P$ (d)	1.48537742	—
$q$	0.418	± 0.003
$a \sin i$	13.67	± 0.05
$M_1 \sin^3 i M_\odot$	10.97	± 0.13
$M_2 \sin^3 i M_\odot$	4.58	± 0.04
$V_\gamma$ (km s <sup>-1</sup> )	26.7	± 2.0

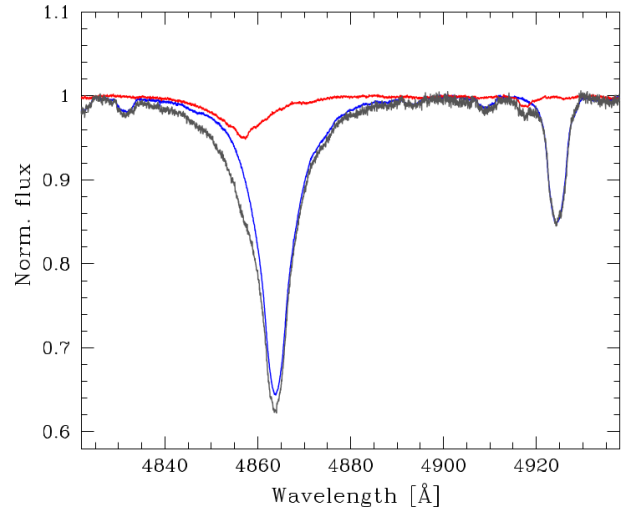


**Figure 11.** Disentangled spectra of the primary component (in solid blue colour) and the secondary component (in solid red colour) superimposed on the observed spectrum of VV Ori in the quadrature (in solid grey). Whilst the He I 4920 Å line is clearly resolved, the broad H $\beta$  line shows only an asymmetric profile, due to unresolved components.

overcomes most of these problems, enabling a simultaneous determination of the orbital parameters, together with a reconstruction of the individual spectra of the components. There is no need for template spectra in this technique, which are usually the main source of uncertainty in RV evaluation by the CCF method. This can come from mismatches in spectral types (Hensberge & Pavlovski 2007). Precision is thus gained in the relative RV values, but the mean motion of the system  $V_\gamma$  has to be determined separately. With disentangling, the components' spectra are effectively separated, which, in turn, permits useful atmospheric diagnostics for either star. This allows a determination of their metallicity values, or detailed abundance signatures. For recent applications of spectral disentangling in complex high-mass binary systems see Pavlovski et al. (2018, 2023), where the methodology used in the present work is described in detail.

Since the FIES, and HERCULES spectra do not cover all the same spectral range, we concentrated on the region where they overlap, i.e. between the H $\gamma$  and H $\beta$  lines. This spectral segment covers about 400 Å and contains various metal lines, the most prominent

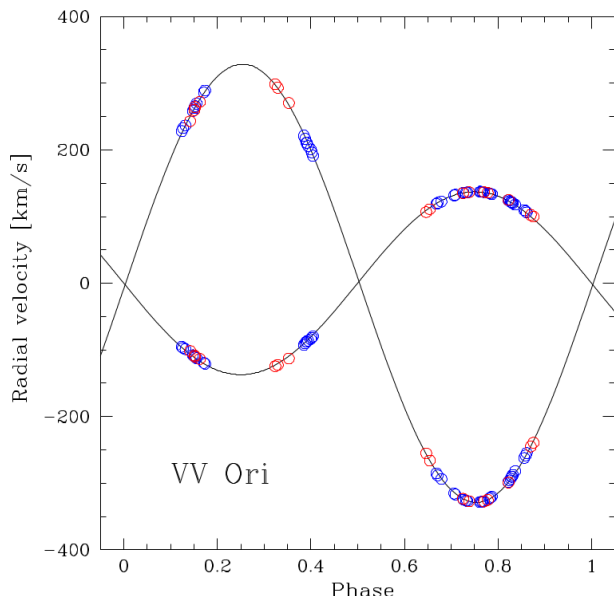


**Figure 12.** The relative radial velocities for the components of VV Ori representing the orbital solution obtained with spectral disentangling (solid black lines). The observations obtained with the FIES spectrograph are shown as open blue circles, while open red ones represent the HERCULES data.

of which is the He I 4471 Å line. As seen in Fig. 11 the helium and metal lines are resolved in the spectra of VV Ori obtained at quadrature. However, in spite of the large RV amplitude of the secondary component (about 660 km s<sup>-1</sup>), Hβ and the other hydrogen lines reflect this only in a changing asymmetry through the course of the orbital cycle. The two main components are never clearly resolved in the Balmer lines. Although spectral disentangling will resolve the hydrogen lines of the primary and secondary, because of the severe blending, precision in determination of the orbital parameters from the H lines is certainly smaller than for the resolved helium and metal lines.

The third body identified through speckle interferometry in the WDS catalogue is approximately 4 mag fainter in V than the primary. It is therefore probably an early A-type main sequence star (Eker et al. 2018) whose observed spectra would show only relatively weak features apart from the Balmer lines. Admission of a third contribution into the modelling at the level of a few % of the main component cannot be definitely confirmed from the residuals in the two component fitting.

The spectral disentangling program specifically referred to in this paper is FDBINARY (Ilijic et al. 2004). This is based on the formulation of disentangling in Fourier space, after Hadrava (1995). Methodological principles concerning disentangling in the wavelength domain are from Simon & Sturm (1994). In FDBINARY Fast Fourier Transforms (FFTs) are used that enable high flexibility in the selection of suitable spectral segments for disentangling whilst maintaining the original spectral resolution.

The RV curves shown in Figure 12 are based on the line-centre wavelength values determined by the line-fitting process. The observed data-points were optimally matched by the theoretical model curve (the continuous lines shown in Figure 12) derived using the RV-curve application of WINFITTER. The corresponding parameters are listed in Table 7. The velocity semiamplitudes ( $K_1$  and  $K_2$ ) are both significantly larger than those inferred from the masses given by Terrell et al. (2007). As a result, the masses we derive are also substantially larger than previously thought.

**Table 8.** The main atmospheric parameters for the components of VV Ori determined by optimal fitting of their disentangled spectra. Also, the fractional light contributions of the components (ldf) can be optimised in an unconstrained mode (see Sect. 3.2).

Parameter	Run 1	Run 2
Primary		
$T_e$ [K]	26 010±320	26 660±300
$\log g$ [cm s <sup>-2</sup> ]	3.96 ± 0.02	4.083*
$v \sin i$ [km s <sup>-1</sup> ]	138.4±2.3	151.4±2.5
ldf	0.908±0.007	0.901±0.007
Secondary		
$T_e$ [K]	15 780±420	16 250±410
$\log g$ [cm s <sup>-2</sup> ]	4.29±0.03	4.320*
$v \sin i$ [km s <sup>-1</sup> ]	89.3±3.1	98.1±3.5
ldf	0.096±0.008	0.095±0.008

### 3.2 Atmospheric parameters

Once individual components' spectra have been separated they can be used for detailed spectroscopic analysis as single star spectra. The disentangled spectra still refer to the common continuum of the binary, hence they are diluted by the fractional light contribution of either component to the total light of the system. Generally, there are two options at this point: (i) disentangled spectra might be first re-normalized to their own continua, using the light ratio determined by other means, i.e. LC analysis (Pavlovski & Hensberge 2010), or (ii) the analysis could be performed directly on the disentangled spectra, since these spectra contain information on the light ratio (Tamajo et al. 2011). It has been shown that uncertainties in the determination of the light ratio from disentangled spectra are comparable to the uncertainties achieved in photometric analysis, and are typically on the order of 1 percent (Pavlovski et al. 2009, 2018, 2022, 2023). In the present work, we decided on the second option, in which the light ratio pertaining to the spectral segment studied would be determined simultaneously with the atmospheric parameters.

The optimal fitting of our disentangled spectra was performed by an extensive search through a pre-calculated grid of theoretical spectra. As a fitting merit indicator we used the sum of squared residuals between the disentangled spectrum and the selected synthetic spectrum using the STARFIT (Kolbas et al. 2014) code. The search procedure is performed by a genetic algorithm, that is based on the PIKAIA subroutine of Charbonneau (1995). The uncertainties are calculated using a Markov Chain Monte Carlo (MCMC) procedure (Ivezić et al. 2014).

Since, in a close binary system, the sum of the fractional light contributions of both components should be unity, we would normally constrain the optimal fitting of the disentangled spectra with that condition. However, as discussed above, there are indications of a faint companion to the close pair in VV Ori. We therefore performed the optimal fitting in an unconstrained mode to allow for a light contribution of such a third star. The result of the modelling, with all atmospheric parameters and fractional light contributions left free, are given in Table 8. Model fits can be seen in Fig. 13.

The sum of the light dilution factors (ldf), i.e. the fractional light contributions of the components to the total light of the system, determined by our optimal fitting of disentangled components' spectra then became slightly larger than unity, thus denying any significant light contribution from a third component. This finding does not support the results of the LC analysis in the present work.

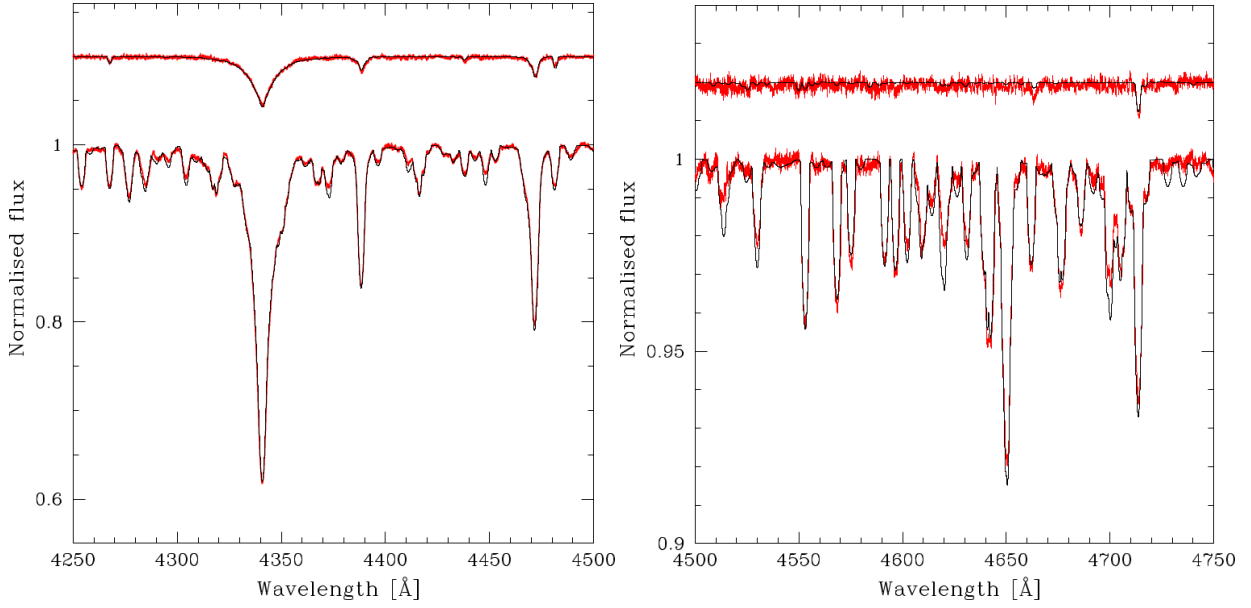


**Figure 13.** Optimal fitting of disentangled spectra for the primary component (lower) and secondary component (upper). Disentangled spectra are in red, optimal fits in black. The region of the spectra centred on the H $\gamma$  line (left panel) and various metal lines in the spectral range from  $\lambda$  4500 - 4750 Å (right panel) are shown.

In the LC analysis of BVR photometry of VV Ori (Table 3), and the TESS observations (Table 5) a small third light appeared, in agreement with the astrometric findings of Horch et al. (2017). The light ratio of the main components we derived from the foregoing spectroscopic analysis, however,  $l_{r_{sp}} = l_2/l_1 = 0.106 \pm 0.009$  is in reasonably good agreement with Terrell et al.’s photometric light ratio in the B and b passbands, i.e.  $l_{r_{ph}} = 0.093 \pm 0.001$ , and  $0.098 \pm 0.001$ , respectively.

The eclipsing, double-lined spectroscopic binary nature of VV Ori’s close pair allows determination of their masses and radii with high precision. Since one of the main obstacles in determination of the atmospheric parameters from hydrogen line profiles is degeneracy between the  $T_e$  and surface gravity, a determination of the latter from the system’s dynamics could be used to lift this degeneracy. In the second run of the optimal fitting of the disentangled components’ spectra, the surface gravity values for both components were fixed to those determined from combined spectroscopic and LC analyses. The results of Run 2 with  $\log g$ ’s thus fixed, as indicated by an asterisk, are given in Table 8. Breaking the degeneracy in the  $T_e$  and  $\log g$  parameters has significant effects on the  $T_e$  values. These turn out to be about 650, and 250 K higher than the first run estimates for the primary and secondary components, respectively.

The primary’s  $T_e$  determined by Terrell et al. (2007) was  $T_{e,1} = 26\,200$  K. This is in fair agreement with our determinations in both runs. This finding is encouraging, since Terrell et al. (2007) based the value of the primary’s  $T_e$  on their de-reddened B-V, using an estimate of the interstellar reddening from Na I lines. Older estimates of the  $T_e$  for the primary component (Table 1) were based on Eaton (1975), who found  $T_{e,1} = 25\,400 \pm 1500$  K from modelling the spectral energy distribution in the UV.

### 3.3 Rotational velocities

If the resolution is sufficiently high, spectral line profiles can be modelled with a parameter set that determines the source’s rotation rate and scale of turbulence in the surrounding plasma, as well as the

**Table 9.** Line-modelling parameters for VV Ori averaged from out-of-eclipse observations (see Section 3.3 for explanation of the parameters).

Parameter	primary	$\pm$	secondary	$\pm$
$U$	0.954	0.001	0.955	0.001
$I_0$	-0.101	0.004	-0.018	0.002
$v_{\text{rot}}$ km s $^{-1}$	147.1	5.7	86.1	10.3
$s$ km s $^{-1}$	5.6	2.3	34.3	1.6
$\Delta f$	0.007		0.007	
$\chi^2/\nu$	1.0		0.93	

**Table 10.** Rotational velocities: observed and calculated

	Primary	Secondary
$v \sin i$	$138.4 \pm 2.3$	$89.3 \pm 3.1$
$v_{\text{sync}}$	$176.8 \pm 0.8$	$86.4 \pm 1.7$

wavelength of the centre of light. Such modelling has been carried out in numerous previous studies (Shajin & Struve 1929; Huang & Struve 1954; Slettebak 1985; Butland et al. 2019). The profiles of the He I lines in our high-dispersion spectral images, particularly the  $\lambda 6678$  feature, are well suited to this purpose.

The entries in Table 9 follow a similar arrangement to the other tables of model-fitting in this paper.  $U$  refers to the continuum reference level at the line’s central wavelength corresponding to the example shown in Fig. 14. The local continuum is assumed to be a straight line, but it may have a definite slope in the raw data that is empirically dealt with in the fitting procedure. The quantities  $I_0$  correspond to the central depths relative to the local continuum (average of the six profiles examined). The equatorial rotational velocity of the primary  $v_{\text{rot},1}$  is calculated with an inclination  $i = 79.0^\circ$  (Table 5) to correct for the projection. The parameter  $s$  relates to the

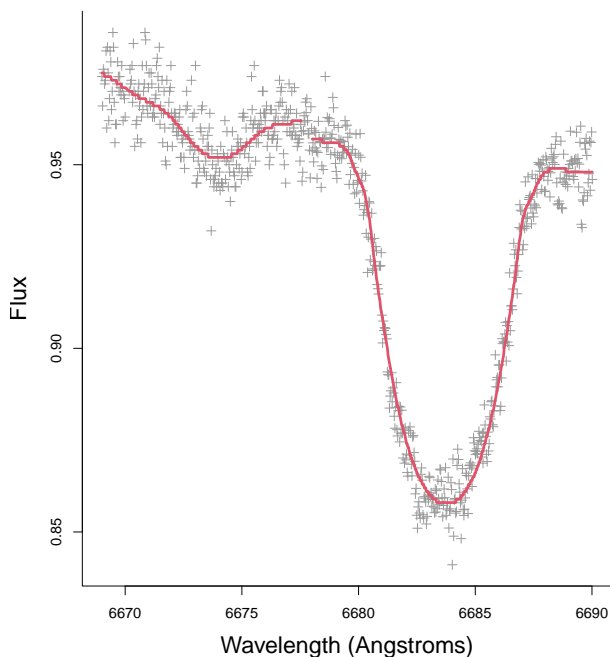


**Figure 14.** Profile fitting to the He I  $\lambda 6678$  lines: The lines have been fitted separately and do not quite return to the same sloping continuum level.

scale of gaussian broadening that is convolved with that from the rotation. It may be interpreted as a measure of the turbulence of the source plasma, or perhaps some other near-symmetric broadening effect. The conspicuous, and consistently obtained high value of this parameter for the secondary (compared to the primary) is noteworthy.  $\Delta f$  indicates the standard deviation of raw measures in the data sample.

For synchronized rotation with aligned axes we would expect the projected equatorial speed of the primary, using Table 10, to be  $\sim 0.368 \times 466 / \sin i \text{ km s}^{-1}$ , i.e.  $\sim 175 \text{ km s}^{-1}$ , but from Table 9 it is seen that the observed speed of  $147 \text{ km s}^{-1}$  is significantly less than that. The ratio of the two rotational speed estimates ( $\sim 0.59$ ) is also significantly different to that of the ratio of radii following from Table 5 (0.492). In fact, if we divided the secondary’s rotational velocity by that ratio we would obtain the synchronous rotation value  $175 \text{ km s}^{-1}$  for the primary, i.e. the mean rotational speed of the secondary is close to synchronism, unlike the primary.

Following the discussion of Southworth et al. (2021), this can be interpreted as a non-alignment of the primary’s rotation and orbit axes, that would correspond to an obliquity angle ( $\epsilon$ ) at zero precession angle ( $\psi$ ) of around  $33^\circ$ . Precession of this spin axis could cause the apparent variation of inclination reported by Southworth et al. (2021).

### 3.4 Elemental abundances for the primary component

As the primary component contributes most of the light from this binary, it has more weight in the spectral disentangling. The S/N of the primary’s disentangled spectrum is thus relatively high. This is an important point for detailed abundance analysis. Our adopted procedure is fully described in Pavlovski et al. (2018, 2023). A

**Table 11.** Photospheric elemental abundances for the primary component in VV Ori. For comparison, abundances determined for B-type stars in the Ori I association in Nieva & Simón-Díaz (2011) (abbreviated NSD) are also presented. The elemental abundances for species X is given relative to the hydrogen abundance,  $\epsilon(X) = \log(X/H) + 12$ . The N/O and N/C abundance ratios are also given, as a sensitive probe to mixing processes in the stellar interiors.

Element	This work [dex]	NSD [dex]
C	$8.28 \pm 0.06$	$8.35 \pm 0.03$
N	$7.77 \pm 0.07$	$7.82 \pm 0.07$
O	$8.76 \pm 0.07$	$8.77 \pm 0.03$
Mg	$7.64 \pm 0.06$	$7.57 \pm 0.06$
Si	$7.51 \pm 0.08$	$7.50 \pm 0.06$
Al	$6.41 \pm 0.08$	-
N/O	$-0.99 \pm 0.10$	$-0.95 \pm 0.08$
N/C	$-0.51 \pm 0.09$	$-0.53 \pm 0.08$

grid of NLTE (non-local thermodynamic equilibrium) synthetic spectra is calculated using the programs DETAIL and SURFACE with model atmospheres first produced by ATLAS9 using the LTE (local thermodynamic equilibrium) prescription. Theoretical spectra are broadened according to a given instrumental profile and projected rotational velocity. Abundances are then determined from line profile fittings of the normalised disentangled spectrum of the primary to the adjustable theoretical one.

The following species were considered: C, N, O, Mg, Si, and Al. The microturbulent velocity,  $\xi = 2 \pm 1 \text{ km s}^{-1}$ , is determined from the oxygen lines, which appear to be the most numerous in the primary’s spectrum. The result of the abundance analysis is given in Table 11. Determined abundances are in excellent agreement with previous analyses of high-mass stars in detached binary systems (see Pavlovski et al. 2018, 2023). There has been no previous abundance analysis specifically for VV Ori, but stars in the Ori I association have been extensively studied through recent decades (cf. Simón-Díaz 2010; Nieva & Simón-Díaz 2011, and references therein). Clearly, the elemental abundances, and nitrogen-to-oxygen (N/O) and nitrogen-to-carbon (N/C) abundance ratios for the primary component in VV Ori is the same as for stars in the Ori I association, within the given uncertainties.

## 4 ABSOLUTE PARAMETERS

It is well known that the actual sizes of the component stars in an eclipsing binary system (radii  $R_1$ ,  $R_2$ ) can be determined by combining the results of LC and RV curve parametrization — the ‘eclipse’ or ‘Russell’s’ method. The absolute size of the orbit comes from dividing the RV parameter  $a \sin i$  by  $\sin i$ , using the inclination  $i$  from the LC modelling. The sought radii are simply the product of  $a$  and the fractional radii  $r_{1,2}$ . Surface gravities ( $g_{1,2}$ ), are scaled from the solar value ( $\log g_\odot = 4.437$ ) using the radii and masses  $M_{1,2}$  similarly derived from the combined RV and LC parameters, or using Kepler’s third law, given the period  $P$  and separation  $a$  of the two stars.

We thus determined the physical properties of VV Ori from the photometric results of Section 2 and the spectrometry of Section 3. For this we have used the JKTEBDDIM code (Southworth et al. 2005), modified to apply the IAU system of nominal solar values (Prša et al. 2016), together with the NIST 2018 values for the Newtonian

**Table 12.** Adopted absolute parameters of VV Ori, derived from the combined photometric and spectroscopic analyses discussed in Sections 2 and 3. The units labelled with an ‘N’ are given in terms of the nominal solar quantities defined in IAU 2015 Resolution B3 (Prša et al. 2016).

Parameters		Value	Uncertainty
Masses ( $M_{\odot}^N$ )	$M_1$	11.56	0.14
	$M_2$	4.81	0.06
	$M_3$	2.0	0.3
Radii ( $R_{\odot}^N$ )	$R_1$	5.11	0.03
	$R_2$	2.51	0.02
	$R_3$	1.8	0.10
Semi-major axis ( $R_{\odot}^N$ )	$a$	13.91	0.05
Temperatures (K)	$T_{e1}$	26660	300
	$T_{e2}$	16250	420
	$T_{e3}$	10000	1000
Luminosities $\log(L/L_{\odot}^N)$	$\log L_1$	4.07	0.02
	$\log L_2$	2.60	0.06
	$\log L_3$	1.5	0.2
Absolute magnitudes	$M_{\text{bol}1}$	-5.44	0.05
	$M_{\text{bol}2}$	-1.75	0.14
	$M_{\text{bol}3}$	1.1	0.40
Reddening (mags)	$E(B - V)$	0.08	0.03
Gravities ( $\log[g_{\text{cgs}}]$ )	$\log g_1$	4.08	0.05
	$\log g_2$	4.32	0.06
	$\log g_3$	4.25	0.10
Distance (pc)	$\rho$	396	7

gravitational and the Stefan-Boltzmann constants. Error-bars were derived from the perturbation analysis referred to in Section 2.1. The results are given in Table 12.

We calculated a distance to the system using optical  $UBVR$  magnitudes from Ducati et al. (2001), near-IR  $JHK_s$  magnitudes from 2MASS (Cutri et al. 2003) converted to the Johnson system using the transformations from Carpenter (2001), and bolometric corrections from Girardi et al. (2002). The interstellar reddening was determined by requiring the optical and near-IR distances to match. We found a distance of  $396 \pm 7$  pc. This is significantly shorter than the distance of  $441 \pm 22$  pc from the *Gaia* DR3 parallax (Gaia Collaboration et al. 2016, 2018, 2021, 2023). Possible explanations for this are that the *Gaia* parallax was affected by the brightness of the system and/or the presence of the nearby third body. Evidence in support of this comes from the renormalised unit weight error (RUWE) of 1.347 being close to the upper limit of 1.4, beyond which the *Gaia* parallax is considered unreliable<sup>3</sup>.

The photometric parallax ( $\pi$ ) can be derived from the formula (Budding & Demircan, 2007, Eqn 3.42)

$$\log \pi = 7.454 - \log R - 0.2V - 2F'_V, \quad (7)$$

where  $F'_V$  is directly proportional to the logarithm of a star’s mean surface flux (Barnes & Evans 1976), and is specified by  $F'_V = \log T_e + 0.1BC$ , where  $BC$  is the bolometric correction. Applying Eqn 7 directly to the stars in VV Ori, with the  $V$  magnitudes from Section 2, the  $R$  and  $T_e$  values from Table 12, and the  $BC$  values from Budding & Demircan (2007) Table 3.1, we obtain  $\log \pi_1 = -2.64$ , and  $\log \pi_2 = -2.66$ . The third star would also produce a comparable value  $\log \pi_3 \approx -2.7$ , if we put its  $T_e$  at 10000 K, but data on that star

<sup>3</sup> [https://gea.esac.esa.int/archive/documentation/GDR2/Gaia\\_archive/chap\\_datamodel/sec\\_dm\\_main\\_tables/sssec\\_dm\\_ruwe.html](https://gea.esac.esa.int/archive/documentation/GDR2/Gaia_archive/chap_datamodel/sec_dm_main_tables/sssec_dm_ruwe.html)

are still very approximate. These parallaxes are in close agreement with the value cited above from the *Gaia* DR3, but the measured  $B - V$  colour excess argues against adopting the measured  $V$  as unaffected by interstellar absorption. Using the relation of Cardelli et al. (1989) with the reddening  $E = 0.08$ , i.e.  $A_V = 0.26$ , the mean distance turns out to be  $\rho = 396 \pm 7$  pc, in good agreement with the foregoing estimate from the  $V - I$  colour.

Evaluation of the absolute luminosities ( $L_{1,2}$ ) and bolometric magnitudes ( $M_{\text{bol}1,2}$ ) of the component stars requires the  $T_e$  values to be known. These were enumerated from the spectral disentangling results given in Table 8, and checked with the colours derived from Table 2. In these calculations, we adopted the solar calibration values as: effective temperature  $T_e = 5780$  K,  $M_{\text{bol}} = 4.75$  from the IAU-adopted solar constants. The adopted absolute parameters for VV Ori are listed, with their uncertainties, in Table 12.

The parameters of the third star are included in Table 12 for completeness, assuming that it is coeval with the close binary and about 4.5 V mag fainter (Section 1). The third star’s properties should still be regarded as quite imprecise compared with those of the main components. Better knowledge of this wide system (VV Ori AB) can be expected in future high accuracy survey work.

## 5 DISCUSSION

Part of the rationale for this study was the ongoing programme of precise quantification of stellar properties, using modern data and analysis techniques. We have shown that independent use of two different LC analysis procedures on recent datasets from the TESS programme resulted in very similar values for the main geometric parameters. Combining these parameters with the RV analysis on high-dispersion FIES and HERCULES spectrograms, then recovers absolute parameter sets that are within reasonable error estimates of each other. This bolsters confidence in the employed analytical methods, and provides reliable evidence to check against theory. Fig. 15 shows such a comparison. The MESA Isochrones and Stellar Tracks MIST facility (Dotter 2016; Choi et al. 2016) based on the MESA models (Paxton et al. 2011) was used to plot evolutionary tracks and isochrones for comparison with our derived parameters. The masses and luminosities are in close agreement with corresponding models at a log age (in yr) of  $\sim 6.9$ .

Our results confirm that VV Ori is a young binary system and shares properties with other members of the Orion Ib OB star association, with an age between about 6 and 10 Myr. We confirm a photometric distance of around 400 pc: closer to the value ( $\sim 360$  pc) of Brown et al. (1994) for the Ib subgroup, but lower than the distance ( $\sim 500$  pc) of Warren & Hesser (1978). The *Gaia* DR3 value ( $\sim 440$  pc) was considered relatively imprecise, perhaps due to calibration difficulties for this bright star in a crowded field containing nebosity. Post-*Gaia* population studies (Zari et al. 2019) have identified substructures within the Orion Ib Association (see also Warren & Hesser, 1977; 1978). Interestingly, the galactic coordinates of VV Ori would place it in the B7, or, marginally, the E subgroup, which has an estimated mean age of close to 11 Myr.

In Section 4 we have given the log age value as  $\approx 6.9$ , supporting the idea that VV Ori is slightly older than the bulk of the  $\epsilon$  Ori association (see Fig. 1). The age of 8 My is, however, young enough to fall within Zahn’s (1977) synchronization timescale for massive stars with radiative envelopes and initial separations of around  $20 R_{\odot}$ .

In this context, it may be possible to form an independent assessment of the age by referring to the estimated synchronization

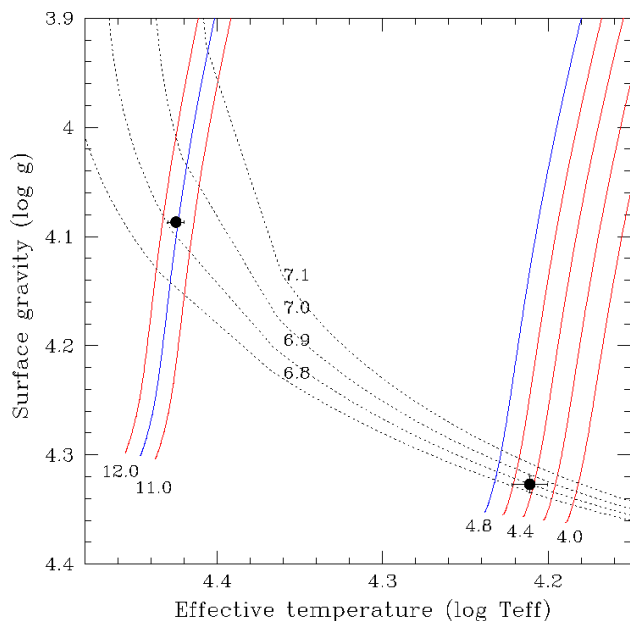


**Figure 15.** Derived  $\log T_e$  and  $\log g$  parameters (Table 12) with their uncertainties for the close pair in VV Ori (filled black circles) are compared with the MIST evolutionary tracks and isochrones (Dotter 2016; Choi et al. 2016). The near-vertical evolutionary tracks are labelled according to masses in  $M_\odot$ . Blue curves are close to the adopted values. Isochrones (dotted) are given in logarithm of time in yr.

time-scales. The observed  $v \sin i$ , and synchronized velocities are given in Table 10. The observed rotational velocity of the primary appears low by  $\sim 40 \text{ km sec}^{-1}$ . The secondary’s rotational velocity is, on the other hand, in good agreement with a synchronized state. The low width of the primary’s line core implies that any additional broadening effect, such as macro-turbulence, would not improve agreement between the observed primary rotation and the value corresponding to synchronization.

This low value of the apparent rotation is, however, in keeping with the possibility of a displaced spin axis raised in Section 2.2. Given the report of changes in the apparent inclination (Southworth et al. 2021) and keeping in mind the interaction between the heat-transfer driven  $\beta$  Cep pulsations and tides (Townsend et al. 2018; Pedersen 2022), the phenomenon of precession can resolve the various observed oddities of the system. The dynamics of this situation then invites critical attention from relevant theory.

Here we may note that a major source of uncertainty in modelling stellar structure and pulsation properties of upper main sequence stars is the distribution and transport of internal angular momentum. Asteroseismology allows for the determination of the interior rotation of stars, provided non-radial oscillations are present at a suitable level. Normal modes of oscillation, calculated for non-rotating, single stars, become split by rotation and tidal distortions.

Four main processes have been taken to contribute to angular momentum transport within stellar radiative regions: meridional circulation, turbulence driven by instabilities, magnetism, and internal waves (Goldreich & Nicholson 1989; Zahn 2013; Mathis 2013). During core hydrogen and helium burning phases, single stars are expected to rotate nearly uniformly. However, in a binary system, even during early phases of evolution, tidal interactions may give rise to non-uniform rotation. In particular, differential rotation in radiative envelopes can induce a diversity of hydrodynamical and

magnetohydrodynamical instabilities, that will, in turn, transport and redistribute angular momentum. The secondary component of VV Ori appears to be in near-synchronous rotation, so we expect that differential rotation in that star to be relatively unimportant in comparison with that of the asynchronous primary.

Analysis of the low-order oscillation modes observed in  $\beta$  Cep stars should be able to inform us about the star’s internal structure. Thus, convective overshoot at the convective core/radiative interface is a major source of turbulence. Mixing length theory contains a free parameter which determines the extent of overshoot in terms of the local pressure scale height  $H_p$ . This overshoot region is probed by comparing observed oscillation frequencies with those of models for a range of prescriptions of the overshoot parameter. So, as well as determining the size and location of the convective core, the frequency spectrum reflects conditions around it that bear on the stellar modelling and angular momentum regime.

A potentially important source of angular momentum transport is internal gravity waves (IGW) propagating in the stably-stratified envelope. The generation and damping of these waves depend sensitively on their frequency and length scales. They may be present either at the core-radiative interface, or in thin convection zones near the surface, where local opacity increases in accordance with the  $\kappa$ -mechanism, or else by tidal forcing (Zahn 1975). For the latter, tidal forces generate a disturbance at the interface that propagates away from the core. Such waves are large scale  $l = 2$ ,  $m = 1$  or 2 and have frequency equal to the forcing frequency  $\sigma$  (in the co-rotating frame). In a rotating star,  $\sigma = k\Omega_{\text{orb}} - m\Omega$ , where  $\Omega_{\text{orb}}$  is the orbital frequency and  $\Omega$  that of the rotation; while  $k > 0$  and  $m$  ( $|m| \leq l$ ) are integers. Dissipation of these waves occurs by non-adiabatic thermal damping effects near the surface of the star. This is different for prograde ( $m > 0$ ) and retrograde ( $m < 0$ ) waves, thus giving rise to a net transport of angular momentum. In this way, IGWs couple convective core and radiative envelope regions, and from asteroseismic data it appears that this coupling is strong.

However, the exact quantification of such conditions from seismic analysis appears still unsettled regarding modelling or observational data selections, with implications on the confidence of interpretation (Salmon et al. 2022). In particular, models that include rotation and/or tidal distortions are not yet directly available.

One source of uncertainty is the extent of chemical mixing which, in young intermediate to high-mass stars arises from instabilities in the radiative layers and, based on interpretation of asteroseismic data, is orders of magnitude lower than expected. Chemical gradients at the core-envelope interface should develop as the star evolves and affect the amplitudes of low-frequency  $g$ -mode waves.

With regard to magnetic fields transporting angular momentum, these may be thought to be largely confined to the convective core (MacGregor & Cassinelli 2003), though other convective zones near the surface would generate fields that could transmit angular momentum along connecting field lines.

Townsend et al. (2018) have investigated the transport of angular momentum by heat-driven non-radial  $g$ -modes, producing a table of models covering most of the mass range of young B-type stars. From their Fig 7, it can be seen that both VV Ori’s primary and secondary (Table 12) are on the edge of the region in the HR diagram, in which their torque instability operates. While this may suggest that the proposed mechanism is not viable, the model does not include the effects of tides or rotation. Moreover, Townsend et al. assumed aligned spin and orbital axes, whereas with the putative precession in VV Ori this would not be the case. One of the effects of non-alignment would be that the  $m = \pm 1$  modes would also con-

tribute to angular momentum transport in the radiative region, in addition to the  $m = \pm 2$  modes (for the dominant  $l = 2$  tide).

Clearly, the effects of tides and rotation on the instabilities that give rise to these waves need to be investigated before any definitive predictions can be made. Meanwhile, the juxtaposition of the properties of the stars in VV Ori, as determined from the classical methods reported in this paper, against asteroseismological inferences should have very interesting consequences.

**6 ACKNOWLEDGEMENTS**

Generous allocations of time on the 1m McLennan Telescope and HERCULES spectrograph at the Mt John University Observatory in support of the Southern Binaries Programme have been made available through its TAC and supported by its Director, Dr. K. Pollard and previous Director, Prof. J. B. Hearnshaw. Useful help at the telescope was provided by the MJUO management (N. Frost and previously A. Gilmore & P. Kilmartin). Considerable assistance with the use and development of the HRSP software was given by its author Dr. J. Skuljan, and very helpful work with initial data reduction was carried out by R. J. Butland.

This work was based on observations made with the Nordic Optical Telescope, owned in collaboration by the University of Turku and Aarhus University, and operated jointly by Aarhus University, the University of Turku and the University of Oslo, representing Denmark, Finland and Norway, the University of Iceland and Stockholm University at the Observatorio del Roque de los Muchachos, La Palma, Spain, of the Instituto de Astrofísica de Canarias.

General support for this programme has been shown by the School of Chemical and Physical Sciences of the Victoria University of Wellington; as well as the Çanakkale Onsekiz Mart University, Turkey, notably Prof. O. Demircan. The Royal Astronomical Society of New Zealand, particularly its Variable Stars South section (<http://www.variablestarssouth.org>), was also supportive.

It is a pleasure to express our appreciation of the high-quality and ready availability, via the Mikulski Archive for Space Telescopes (MAST), of data collected by the TESS mission. Funding for the TESS mission is provided by the NASA Explorer Program. This research has made use of the SIMBAD data base, operated at CDS, Strasbourg, France, and of NASA’s Astrophysics Data System Bibliographic Services. We thank the University of Queensland for the use of collaboration software. We are grateful for the helpful comments and guidance by the anonymous referee, which led to an improved paper.

**7 DATA AVAILABILITY**

The TESS photometric data used in this study are publicly available from the Barbara A. Mikulski Archive for Space Telescopes (MAST) portal maintained by the Space Telescope Science Institute. The BVR photometric data underlying this article will be shared on reasonable request to M. Blackford and also available as supplemental material to the electronic version of the paper. HERCULES spectroscopy can be sourced from E. Budding. FIES spectra can be obtained from K. Pavlovski, J. Southworth, or the NOT archive at <https://www.not.iac.es/archive/>.

**Table A1.** Significant peaks in VV Ori frequency spectrum.

Freq. d <sup>-1</sup>	Ampl. (mmag)	Phase (rad)
0.0042 ± 0.0000	11.4053 ± 0.0047	0.7062 ± 0.0001
0.1166 ± 0.0001	1.1453 ± 0.0047	0.7511 ± 0.0007
0.2353 ± 0.0010	0.1014 ± 0.0047	0.7168 ± 0.0074
0.3087 ± 0.0012	0.0816 ± 0.0047	0.6794 ± 0.0092
0.4459 ± 0.0015	0.0674 ± 0.0047	0.0007 ± 0.0112
0.5902 ± 0.0012	0.0862 ± 0.0047	0.3041 ± 0.0087
0.6696 ± 0.0006	0.1589 ± 0.0047	0.6249 ± 0.0047
0.7776 ± 0.0013	0.0797 ± 0.0047	0.4689 ± 0.0095
0.8196 ± 0.0011	0.0948 ± 0.0047	0.7560 ± 0.0079
1.1574 ± 0.0016	0.0615 ± 0.0047	0.1898 ± 0.0122
1.3075 ± 0.0003	0.2899 ± 0.0047	0.6053 ± 0.0026
1.4047 ± 0.0007	0.1513 ± 0.0047	0.4425 ± 0.0050
1.6139 ± 0.0016	0.0631 ± 0.0047	0.1496 ± 0.0119
1.9836 ± 0.0015	0.0683 ± 0.0047	0.3762 ± 0.0110
2.5417 ± 0.0009	0.1099 ± 0.0047	0.9549 ± 0.0069
2.7875 ± 0.0011	0.0897 ± 0.0047	0.4184 ± 0.0084
2.8376 ± 0.0004	0.2318 ± 0.0047	0.8943 ± 0.0033
4.0018 ± 0.0009	0.1075 ± 0.0047	0.2149 ± 0.0070
4.7099 ± 0.0010	0.1028 ± 0.0047	0.1232 ± 0.0073
5.3827 ± 0.0006	0.1798 ± 0.0047	0.0331 ± 0.0042
5.4875 ± 0.0014	0.0731 ± 0.0047	0.9579 ± 0.0103
5.6319 ± 0.0008	0.1216 ± 0.0047	0.4694 ± 0.0062
7.1503 ± 0.0008	0.1283 ± 0.0047	0.9558 ± 0.0059
7.6831 ± 0.0008	0.1243 ± 0.0047	0.9236 ± 0.0061
7.8308 ± 0.0003	0.3680 ± 0.0047	0.8973 ± 0.0020
8.0721 ± 0.0017	0.0600 ± 0.0047	0.1402 ± 0.0126
8.3589 ± 0.0005	0.1973 ± 0.0047	0.1094 ± 0.0038
8.4197 ± 0.0014	0.0718 ± 0.0047	0.7448 ± 0.0105
8.4772 ± 0.0011	0.0930 ± 0.0047	0.5730 ± 0.0081
8.5029 ± 0.0005	0.1847 ± 0.0047	0.6060 ± 0.0041
8.7186 ± 0.0015	0.0690 ± 0.0047	0.0109 ± 0.0109
9.0322 ± 0.0002	0.5902 ± 0.0047	0.2577 ± 0.0013
9.0958 ± 0.0013	0.0753 ± 0.0047	0.3013 ± 0.0100
9.1773 ± 0.0001	1.4365 ± 0.0047	0.2618 ± 0.0005
10.0176 ± 0.0013	0.0754 ± 0.0047	0.4459 ± 0.0100
10.3193 ± 0.0009	0.1093 ± 0.0047	0.8415 ± 0.0069
10.3798 ± 0.0001	1.2726 ± 0.0047	0.0622 ± 0.0006
10.4817 ± 0.0015	0.0656 ± 0.0047	0.7674 ± 0.0115
11.0542 ± 0.0008	0.1322 ± 0.0047	0.1982 ± 0.0057
11.1685 ± 0.0004	0.2789 ± 0.0047	0.1763 ± 0.0027
11.2012 ± 0.0003	0.3549 ± 0.0047	0.7060 ± 0.0021
11.7989 ± 0.0006	0.1617 ± 0.0047	0.7024 ± 0.0047
11.8698 ± 0.0001	0.9092 ± 0.0047	0.4085 ± 0.0008
13.0721 ± 0.0002	0.5211 ± 0.0047	0.6850 ± 0.0014
13.2177 ± 0.0002	0.5919 ± 0.0047	0.1865 ± 0.0013
13.7346 ± 0.0014	0.0715 ± 0.0047	0.9988 ± 0.0105
13.8899 ± 0.0005	0.1992 ± 0.0047	0.3467 ± 0.0038
14.3084 ± 0.0013	0.0772 ± 0.0047	0.0037 ± 0.0098
14.4155 ± 0.0009	0.1104 ± 0.0047	0.9842 ± 0.0068
14.5005 ± 0.0016	0.0612 ± 0.0047	0.2587 ± 0.0123
14.5623 ± 0.0004	0.2594 ± 0.0047	0.0344 ± 0.0029
15.2349 ± 0.0012	0.0842 ± 0.0047	0.6404 ± 0.0089
20.9609 ± 0.0009	0.1082 ± 0.0047	0.5285 ± 0.0078
22.3940 ± 0.0010	0.0975 ± 0.0047	0.7536 ± 0.0077
23.5953 ± 0.0007	0.1417 ± 0.0047	0.0482 ± 0.0053
25.0870 ± 0.0006	0.1600 ± 0.0047	0.3657 ± 0.0047
25.7319 ± 0.0020	0.0511 ± 0.0047	0.9643 ± 0.0148
26.2917 ± 0.0012	0.0807 ± 0.0047	0.6437 ± 0.0093
27.7816 ± 0.0014	0.0697 ± 0.0047	0.9514 ± 0.0108

**Table A2.** Identified spectral lines for VV Ori (p ≡ primary; s ≡ secondary).

Species	Order no.	Adopted $\lambda$	Comment
He I	85	6678.149	well-defined p; s weak, noisy
H $\alpha$	87	6562.817	s noticeable in p profile
He I	97	5875.340	well-defined p; s weak
Na II	97	5895.923	deep, narrow structured D-lines
Na II	97	5889.953	—
Si III	99	5739.620	p & s visible
C III	100	5696.00	p only
N II	100	5679.56	
Si II	101	5639.49	
C III	109	5217.93	
O II	109	5206.73	
He I	112, 113	5047.736	p strong, s visible
He I	113	5015.675	p only
N II	114	5001.30	
O II	115	4942.1	blend
C III	115	4922.14	
H $\beta$	117	4861.332	s visible but blended
C III	118	4819.63	p blend
N II	121	4718.4	weak
He I	120, 121	4713.258	weak p & s
O II	121	4699.21	
He II	122	4685.682	p only
O II	122	4674.213	
C III	122	4663.53	
C III	122	4650.160	
C III+ OII	123	4649.86	strong blend
N II	123	4630.567	
N II	123	4621.39	
O II	123	4610.14	
O II	124	4602.11	
O II	124	4596.174	
C III	124	4593.47	
Si III	125	4574.78	edge of order
Si III	125	4569.67	blend
C III	125	4567.872	
Si III	125	4552.65	blend

**REFERENCES**

- Aerts C., Christensen-Dalsgaard J., Kurtz D.W., 2010, *Asteroseismology*, Springer Dordrecht, ISBN, 978-1-4020-5178-4, <https://doi.org/10.1007/978-1-4020-5803-5>
- Barnes, T.G., Evans, D.S., 1976, *MNRAS*, 174, 489
- Barr J.M., 1905, *Selected Papers and Proc. Roy. Astron. Soc. Canada*, 1904, 42
- Beltrami G., Galeotti P., 1969, *IAU Inform. Bull. Var. Stars*, 393, 1
- Bevington P. R., 1969, *Data Reduction and Analysis for the Physical Sciences*, McGraw-Hill, New York
- Blackford M. G., Erdem A., Sürgit D., Özkardeş B., Budding E., Butland R., Demircan O., 2019, *MNRAS*, 487, 161
- Blaauw A., 1964, *ARA&A*, 2, 213
- Bowman D.M., 2020, *Front. Astron. Space Sci.*, 7, 70
- Bowman D.M., Johnson C., Tkachenko A., Mkrtychian D.E., Gunsriwiwat K., Aerts C., 2019, *ApJL*, 883, L26
- Brown A.G.A., de Geus E.J., de Zeeuw P.T., 1994, *A&A*, 289, 101
- Budding E., Demircan O., 2007, *Introduction to Astronomical Photometry*, Cambridge University Press, ISBN: 9780511536175
- Budding E., Demircan O., 2022, *A Guide to Close Binary Systems, Series in Astronomy & Astrophysics*, Taylor & Francis Limited, ISBN: 9781138064386
- Budding E., Najim N.N., 1980, *Astrophys. Space Sci.*, 72, 369
- Budding E., Love T., Blackford M.G., Banks T., Rhodes M.D., 2021, *MNRAS*, 502, 6032
- Burssens S. et al., 2020, *A&A*, 639, 81
- Butland R.J., Erdem A., Özkardeş B., Blackford M.G., Sürgit D., Budding E., Demircan O., 2019, *MNRAS*, 482, 2644
- Cardelli J. A., Clayton G. C., & Mathis J. S., 1989, *ApJ*, 345, 245
- Carpenter J.M., 2001, *AJ*, 121, 2851
- Chambliss C.R., 1983, *Astrophys. Space Sci.*, 89, 15
- Chambliss C.R., 1984, *Astrophys. Space Sci.*, 99, 163
- Chambliss C. R., Davan B. M., 1987, *AJ*, 93, 950
- Chambliss C. R., Leung K.-C., 1982, *ApJS*, 49, 531
- Charbonneau P., 1995, *ApJS*, 101, 309
- Choi J., Dotter A., Conroy C., Cantiello M., Paxton B., Johnson B. D., 2016, *ApJ*, 823, 102
- Clausen J.V., 1996, *A&A*, 308, 151
- Cokina M., Maslej-Kresnáková V., Butka P., Stefan Parimucha S., 2021 *ArXiv*, 2108.01640
- Cutri R. M., et al. 2003, *Explanatory Supplement to the 2MASS All Sky Data Release* (Washington: NASA), <http://www.ipac.caltech.edu/2mass/releases/allsky/doc/explsup.html>
- Daniel Z., 1915, *Publ. Allegheny*, 3, 179
- Desnoux V., Buil C., 2005, *Soc. Astron. Sci. Ann. Symp.*, 24, 129
- Dotter A., 2016, *ApJS*, 222, 8
- Ducati J. R., 2002, *CDS/ADC Collection of Electronic Catalogues*, 2237
- Ducati J. R., Bevilacqua C. M., Rembold S. B., Ribeiro D., 2001, *ApJ*, 558, 309
- Duerbeck H.W., 1975, *Astron. Astrophys., Suppl. Ser.*, 22, 19
- Eaton J.A., *Astrophys. J.*, 197, 379
- Eker Z. et al., 2018, *MNRAS*, 479, 5491
- Erdem A. et al., 2022, *MNRAS*, 515, 6151
- Feiden G.A., 2015, in “Living Together: Planets, Host Stars and Binaries”, *Proceedings of a conference held 8-12 September 2014 in Litomyšl, Czech Republic*; edited by Rucinski S.M., Torres G., Zejda M., *ASP Conference Series*, Vol. 496, San Francisco: *Astronomical Society of the Pacific*, p.137
- Fuller J., Kurtz D.W., Handler G., Rappaport S., 2020, *MNRAS*, 498, 5730
- Gaia Collaboration, Brown A. G. A., Vallenari A., et al., 2016, *A&A*, 595, A1
- Gaia Collaboration, Brown A. G. A., Vallenari A., Prusti T., et al., 2018, *A&A*, 616, 22
- Gaia Collaboration, Brown A. G. A., Vallenari A., Prusti T., et al., 2021, *A&A*, 694, 1
- Gaia Collaboration, Vallenari A., Brown A. G. A., Prusti T., et al., 2023, *A&A*, 674, 1
- Girardi L., Bertelli G., Bressan A., Chiosi C., Groenewegen M. A. T., Marigo P., Salasnich B., Weiss A., 2002, *A&A*, 391, 195
- Golay M., 1974, *Introduction to Astronomical Photometry*, D. Reidel Publishing Company, Dordrecht, Holland, ISBN: 978-90-277-0428-3
- Goldreich P., Nicholson P.D., 1989, *ApJ*, 342, 1079
- Hadrava, P., 1995, *A&AS*, 498, 5730
- Hambleton K.M. et al., 2013, *MNRAS*, 434, 925
- Handler G., Kurtz D.W., Rappaport S.A., et al., 2020, *Nat Astron*, 4, 684
- Hearnshaw J.B., Barnes S. I., Kershaw G.M., Frost N., Graham G., Ritchie R., Nankivell G. R., 2002, *Exp. Astron.*, 13, 59
- Hensberge H., Pavlovski K., 2007, in *Binary Stars as Critical Tools & Tests in Contemporary Astrophysics*, Eds: Hartkopf, William I. and Harmanec, Petr and Guinan, Edward F., *Proc. IAU Symp.* 240, p. 136
- Horch E. P. et al., 2017, *AJ*, 153, 212 10.3847/1538-3881/aa6749
- Huang S.S., Struve O., 1954, *Ann. d’ap.*, 17, 85
- Ilijic S., Hensberge H., Pavlovski K., Freyhammer L. M., in *Spectroscopically and Spatially Resolving the Components of the Close Binary Stars*, Eds: Hilditch, R. W., Hensberge, H., Pavlovski, K., *Astronomical Society of the Pacific Conference Series*, 318, 111
- İnlek G., Budding E., Demircan O., 2017, *ApSS*, 362, 167
- Ivezić Ž., Connolly A.J., VanderPlas, J.T. Gray A., 2014, *Statistics, Data Mining, and Machine Learning in Astronomy: A Practical Python Guide for the Analysis of Survey Data*, Princeton University Press, Princeton



- Kolbas V., Dervoşođlu A., Pavlovski K., Southworth J., 2014, *MNRAS*, 444, 3118
- Kopal Z., 1959, *Close Binary Systems*, Chapman & Hall, London
- Kurtz D.W. et al., 2020, *MNRAS*, 494, 5118
- Lampens P., 2006, in “Astrophysics of Variable Stars, Pecs, Hungary, 5-10 September 2005”, Eds: Sterken, C. & Aerts, C., ASP Conference Series, Vol. 349, p. 153, San Francisco: Astronomical Society of the Pacific
- Langer D., 2012, *Annual Review of Astronomy and Astrophysics*, 50, 107
- Len P., Breger M., 2004, *Proc. IAU 2004, AUS224*, 786-790
- Lesh J.R., Aizenman M.L. 1978, *Ann. Rev. Astron. Astrophys.*, 16, 215
- MacGregor K.B., Cassinelli J.P., 2003, *ApJ*, 586
- Mathis S., 2013, in *Lecture Notes in Physics*, Berlin Springer Verlag, eds. M Goupil, K Belkacem, C Neiner, F Ligni eres, JJ Green, vol. 865
- Murphy S., 2018, <https://doi.org/10.48550/arXiv.1811.12659>
- Nieva M. F., Sim on-D az S., 2011, *A&A*, 532, A2
- Pavlovski K., Hensberge H., 2010, *Binaries - Key to Comprehension of the Universe*, Eds: Pr sa, A., Zejda, M., Astronomical Society of the Pacific Conference Series, 435, 207
- Pavlovski, K. et al., 2022, *A&A*, 658, A92
- Pavlovski K., Southworth J., Tamajo E., 2018, *MNRAS*, 481, 3129
- Pavlovski K., Southworth J., Tkachenko A., Van Reeth T., Tamajo E., 2023, *A&A*, 671, A139
- Pavlovski K., Tamajo E., Koubsky P., Southworth, J., Yang S., Kolbas V. 2009, *MNRAS*, 400, 791
- Paxton B., Bildsten L., Dotter A., Herwig F., Lesaffre P., Timmes F., 2011, *ApJS*, 192, 3
- Pedersen M.G., 2022, *ApJ*, 940, 49
- Pedersen M.G. et al., *ApJ*, 872, L9
- Popper D. M., 1993, *PASP*, 105, 721
- Pr sa A., et al., 2016, *AJ*, 152, 41
- Ratajczak M., Pigulski A., Pavlovski K., 2017, *Proc. Polish Astronomical Society, Second BRITE-Constellation Science Conf.: Small Satellites—Small satellites — Big Science*, Eds: Zwintz, K, Poretti, E., Warsaw: Polish Astronomical Society, 128
- Rhodes M. D., 2021, *WINFITTER manual*, <https://michaelrhodesbyu.weebly.com>
- Ricker G.R. et al., 2014, *Proc. SPIE* Vol. 9143, doi: 10.1117/12.2063489
- Russell H.M., 1912a, *ApJ*, 35, 315
- Russell H.M., 1912b, *ApJ*, 36, 54
- Russell H.M., 1942, *ApJ*, 95, 345
- Russell H.M., Shapley, H., 1912, *ApJ*, 36, 239
- Salmon S.J.A.J., Eggenberger P., Montalban J., Miglio A., Noels A., Buldgen G, Moyanol F, Meyneti G., 2022, *A&A* 659, A142
- Sana H. et al., 2012, *Science*, 337, 444
- Sarma M.B.K., Vivekananda R.P., 1995, *J. Astrophys. Astron.*, 16, 407
- Shajin G., Struve O., 1929, *MNRAS*, 89, 222
- Simon K. P., Sturm E., 1994, *A&A*, 281, 286
- Sim on-D az S., 2010, *A&A*, 510, A22
- Skuljan J., in “Variable Stars in the Local Group”, IAU Colloquium 193, Proceedings of the conference held 6-11 July, 2003 at Christchurch, New Zealand, Eds: Kurtz, D.W., & Pollard, K.R., ASP Conference Proceedings, p. 575, 310, San Francisco: Astronomical Society of the Pacific
- Skuljan J., 2020, *HERCULES Reduction Software Package (HRSP Version 7)*, private communication
- Slettebak A., 1985, *ApJS*, 59, 769
- Stankov A., & Handler G., 2005, *ApJS*, 158, 193
- Sterne T.E., 1939, *MNRAS*, 99, 451
- Southworth J., 2020, *The Observatory*, 140, 247
- Southworth J., 2021, *Universe*, 7, 369
- Southworth J., Bowman D. M., 2022, *MNRAS*, 513, 3191.
- Southworth J., Maxted P.F.L, Smalley B., 2005, *A&A*, 429, 645
- Southworth J. et al., 2011, *MNRAS*, 414, 2413
- Southworth J., Bowman D. M., Tkachenko A., Pavlovski K., 2020, *MNRAS*, 497, L19
- Southworth J., Bowman D.M., Pavlovski K., 2021, *MNRAS*, 501, 65
- Struve O., Luyten W.J., 1949, *ApJ*, 110, 160
- Tamajo, E., Pavlovski, K., Southworth, J., 2011, * *, A76
- Teltin J.H. et al., 2014, *Astron. Nach.*, 335, 41
- Terrell D., Munari U., Siviero A., 2007, *MNRAS*, 374, 530
- Townsend R.H.D, Goldstein J., Zweibel E.G., 2018, */mnras*, 475, 879
- Van Hamme W., Wilson R.E., 2007, *ApJ*, 661, 1129
- Waelkens C., 1991, *A&A*, 246, 453
- Warren W.H. Jr., Hesser J.E., 1977, *ApJS*, 34, 115
- Warren W.H. Jr., Hesser J.E., 1978, *ApJS*, 36, 497
- Wells D.C., Greisen E.W., Harten R.H., 1991, *A&A Supp.*, 44, 363
- Welsh W.F., Orosz J.A., Aerts C., Brown T.M., et al., 2011, *ApJS*, 197, 4
- Wilson R.E., 1979, *ApJ*, 234, 1054
- Wilson R.E., Devinney E.J., 1972, *ApJ*, 166, 605
- Wilson R.E., Van Hamme W., 2004, *Computing Binary Star Observables (Wilson-Devinney program user guide)*. Available at <ftp://ftp.astro.ufl.edu/pub/wilson>
- Wood F.B., 1946, *Contr. Princeton Univ. Obs.*, 21, 25
- Wright N.J., 2020, *NewAR*, 90, 101549
- Zahn J.-P., 1975, *A&A*, 41, 329
- Zahn J.-P., 1977, *A&A*, 57, 383
- Zahn J.-P., 2013, in *EAS Publications Series*, eds. G Alecian, Y Lebreton, O Richard, G Vauclair, vol. 63
- Zari E., Brown A.G.A., de Zeeuw P.T., 2019, *A&A*, 628, 123
- Zucker C., Alves J., Goodman A., et al., 2023, *Protostars and Planets VII*, ASP Conference Series, Vol. 534, Proceedings of a conference held 10-15 April 2023 at Kyoto, Japan. Edited by Shu-ichiro Inutsuka, Yuri Aikawa, Takayuki Muto, Kengo Tomida, and Motohide Tamura. San Francisco: Astronomical Society of the Pacific, p.43

This paper has been typeset from a  $\text{\TeX}/\text{\LaTeX}$  file prepared by the author.